AGU PUBLICATIONS

Journal of Advances in Modeling Earth Systems

RESEARCH ARTICLE
10.1002/2015MS000560

ITCZ structure as determined by parameterized versus explicit convection in aquachannel and aquapatch simulations

David S. Nolan[1], Stefan N. Tulich[2], and Joaquin E. Blanco[1]

[1]Rosenstiel School of Marine and Atmospheric Science, University of Miami, Miami, Florida, USA, [2]Cooperative Institute for Research in the Environmental Sciences, University of Colorado, Boulder, Colorado, USA

Key Points:
- Aquachannel and aquapatch models can be used to simulate the general circulation on an aquaplanet
- Grid-nesting within an aquachannel can be used to achieve cloud-resolving grid spacings
- Cloud-resolving simulations produce broader rainfall because they have propagating squall lines

Correspondence to:
D. S. Nolan,
dnolan@rsmas.miami.edu

Citation:
Nolan, D. S., S. N. Tulich, and J. E. Blanco (2016), ITCZ structure as determined by parameterized versus explicit convection in aquachannel and aquapatch simulations, *J. Adv. Model. Earth Syst.*, *8*, 425–452, doi:10.1002/2015MS000560.

Received 1 OCT 2015
Accepted 21 JAN 2016
Accepted article online 2 FEB 2016
Published online 22 MAR 2016

Abstract Numerous studies using both global and regional models of the atmosphere have found daunting sensitivities of the structure and dynamics of the intertropical convergence zone (ITCZ) to the representations of unresolved processes, particularly the convective parameterization (CP). Evaluations of these results by comparison to high-resolution simulations with explicit convection have been rather limited, due to the large computational burden of using grid spacings less than 10 km over large domains representative of the Earth's tropics. This study introduces a framework that allows the use of cloud-resolving grid spacings over the tropics and larger spacings over remainder of the domain. The Weather Research and Forecasting (WRF) model is used in an "aquachannel" beta-plane configuration, zonally periodic with length equal to that of the real equator. This model reproduces the general circulation and eddy statistics of similarly configured aquaplanet models. A channel shortened to one third the length of the equator (the "aquapatch") also reproduces the zonal-mean circulations and eddies. Finally, nested grids embedded in the aquapatch are used to simulate tropical convection with 5.15 km resolution. The nested 5.15 km simulations produce broader and lighter rainfall distributions, making single ITCZs wider and smoothing out double ITCZ structures. They also show quite different rainfall production rates for atmospheric parameters such as convective available potential energy (CAPE) and column relative humidity (CRH). The apparent reason for these differences is that the higher resolution allows for the representation of squall lines and associated cold pools that propagate meridionally, redistributing rainfall away from the ITCZ.

1. Introduction

In the present day global climate models (also known as general circulation models, or GCMs) are the most widely used tool for understanding the general circulation and climate of the Earth, and for predicting their changes due to either natural processes or anthropogenic influences [*Manabe and Wetherald* 1975; *Houghton et al*., 1990; *Kirtman et al*., 2013; *Collins et al*., 2013]. For this reason, an understanding of the weaknesses, limitations, and biases of such models is crucial for assigning confidence to climate change predictions, as well as for providing guidance for ongoing model improvements. At the core of most climate models is a set of algorithms and codes that simulate the motions of the atmosphere and its response to thermodynamic forcings from the solar and infrared radiation, heat exchange with the surface, and latent heat release and other effects from clouds [*Randall*, 2000; *Satoh*, 2014].

Since the very first GCMs, a standard test of model performance and behavior has been to replace the oceans and continents of the real Earth with an ocean-like surface with fixed sea surface temperature [*Pike*, 1971; *Held and Suarez*, 1994]. This temperature may be an approximation to the Earth's zonally averaged SST [*Hayashi and Sumi*, 1986], something more idealized [*Neale and Hoskins*, 2001], or even constant across the globe [*Sumi*, 1992; *Kirtman and Schneider*, 2000]. These are commonly known as "aquaplanet" simulations. Even with vaguely Earth-like SST profiles, these simulations usually produce time and zonal mean circulations that strongly resemble those of the Earth. The reliable symmetries and other simplifications of the general circulation on a planet without continents facilitates the understanding of changes in the simulated climate as a function of SST distribution, global mean temperature, or radiative properties of the atmosphere [*Medeiros et al*., 2008, 2014]. Furthermore, there can be significant model-to-model differences in both the mean circulations and their variabilities. Since land interactions and ocean circulation feedbacks are absent, such differences can be ascribed entirely to the atmospheric components of each climate

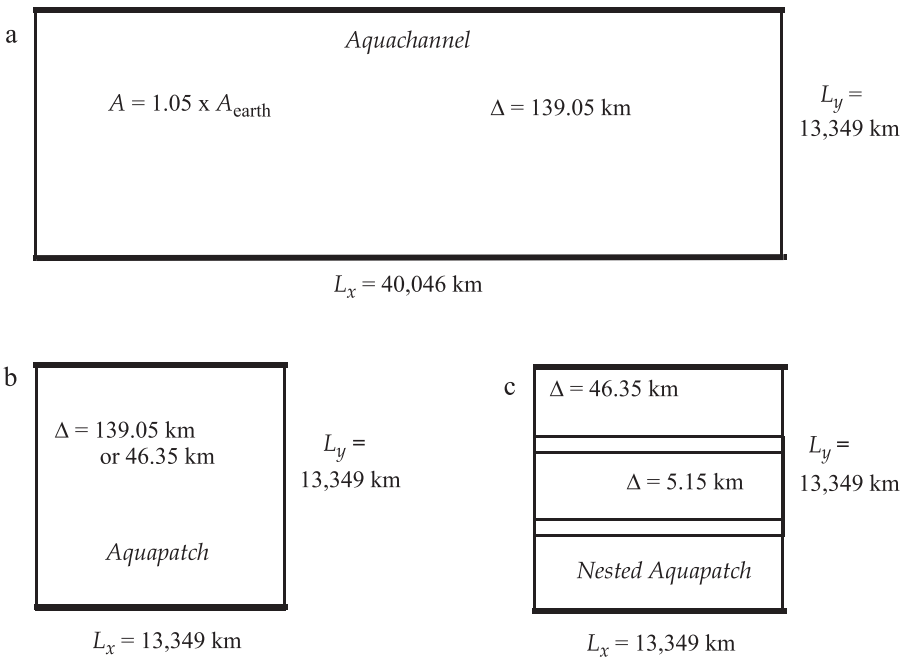

Figure 1. The grid configurations used in this study: (a) the full-length aquachannel; (b) the aquapatch; (c) the aquapatch with nested grids.

model, providing a framework in which such differences can be understood, hopefully leading to model improvements.

Many aquaplanet studies have found the climate of the tropics and particularly the structure and dynamics of the intertropical convergence zone (ITCZ) to be highly sensitive to the parameterization of deep convection (generally known as convective parameterization, hereafter CP; see e.g., *Numaguti* [1995]; *Hess et al.* [1993]; *Liu et al.* [2010]; *Möbis and Stevens* [2012]). Switching between similar CP schemes, or making small changes to a single scheme, can lead to structurally different ITCZs, often demonstrated through the appearance of either a single precipitation maximum at the equator (a single ITCZ) or two distinct maxima on either side of the equator (a double ITCZ).

A desirable test for any CP scheme would be a side-by-side comparison to simulations with sufficiently small grid spacings so that the development of individual convective cells can be reasonably well represented and CP is not necessary. It is generally accepted that such grid spacings must be less than 8 km, and preferably 3 km or less [*Weisman et al.*, 1997; *Pauluis and Garner*, 2006; *Bryan and Morrison*, 2012; *Skamarock et al.*, 2014]. Unfortunately, the very large computational cost of such simulations with model domain sizes similar to the real tropics has been prohibitive for such comparisons, and thus relatively few have been attempted. Global aquaplanet simulations have been performed with the NICAM model [*Satoh et al.*, 2008] using resolutions such as 14 km, 7 km, and 3.5 km [*Nasuno et al.* 2007; *Nasuno*, 2008] and even 0.87 km [*Miyamoto et al.*, 2013]. However, the integration times and usable data provided by these simulations are about 90 days, 30 days, 10 days, and 0.5 days, respectively.

A complicating factor when comparing simulations with CP to cloud-resolving simulations is the fact that increased resolution also likely improves other aspects of a model, such as improving the evolution of mesoscale features and cloud-radiative interactions. It may also degrade other aspects, such as the effects of shallow convection. While the anticipated effects of shallow convection is built into some CP schemes, models with grid spacings greater than 1 km almost certainly do not represent it well [*Bryan et al.*, 2003; *Pauluis and Garner*, 2006].

This paper presents a modeling framework that allows a meaningful comparison between moderate resolution simulations of the tropics with CP and high resolution simulations of the tropics without CP. We use a regional atmospheric model to perform idealized simulations in tropical channel domains with sizes

comparable to the real earth (see Figure 1; more explanation is provided in section 2). The nested grid capability of the model is then used to achieve grid spacings of 5.15 km over a region that is 1/3 the length of the equator, with a spin-up time of 1 year for all simulations and statistics computed over 6 months. Admittedly, 5.15 km resolution would generally not be considered as truly "cloud resolving." However, the cost of increasing resolution further is very large, and the benefit of this marginally cloud-resolving resolution is that it allows us to perform relatively long simulations with satisfactory spin-up and averaging periods.

Although not nearly as common as the aquaplanet configuration, tropical channel models have been used previously to study convection and dynamics in the tropics. *Nolan et al*. [2007, 2010] used a tropical channel configuration in the Weather Research and Forecasting Model (WRF) to study the vertical structure of the ITCZ for various idealized and realistic SST profiles. *Khoudier and Han* [2013] also used WRF to study the effects of CP and resolution on convectively coupled waves. However, their nested domains began and ended inside the outer domain, creating a zonal discontinuity in the physics of the waves. To avoid such problems, *Tulich and Kiladis* [2012] introduced a version of the WRF model where the high resolution grids can be nested inside of each other in the meridional direction, but also extend across zonally periodic boundaries without disruption to the atmospheric flow. Most recently, *Bretherton and Khairoutdinov* [2015] took more of a brute-force approach by using a tropical channel domain with 4 km grid spacing over a domain about half the size of the Earth. The large computational cost limited the period of their simulation to 30 days.

We compare the time and zonal mean circulations of our channel simulations to those produced by various GCMs as part of the "Aqua-Planet Experiment" (APE) described by *Blackburn and Hoskins* [2013], *Blackburn et al*. [2013, hereinafter B13], *Williamson et al*. [2013, hereinafter W13], and *Williamson et al*. [2012, hereinafter the ATLAS]. Despite the very different geometry of the tropical channel domain (i.e., a "flat" world), we will show that the general circulations of our simulations are very similar to those of the aquaplanets.

Our primary finding is that the high resolution simulations without CP generate broader rainfall distributions in the tropics. For broader SST profiles, a distinct double ITCZ, frequently seen in many simulations with CP, does not occur. These differences will be related to the sensitivities of rain production in each model framework to the local atmospheric soundings, which in turn are related to differences in the evolution of convection.

Section 2 describes the model, domains, and parameterizations. Section 3 presents the basic model climatologies and compares them to similar aquaplanet results. The differences between the parameterized and cloud-resolving simulations are studied and understood in section 4. Section 5 provides a summary and some conclusions.

2. Model and Configurations

The atmosphere is simulated with a modified version of the Weather Research and Forecast Model (WRF) version 3.4.1 [*Skamarock et al*., 2008]. The most significant modification of the model is the added capability of nested grids extending around a zonally periodic interface. In standard versions of WRF, nested grids must lie inside of each other and cannot reach to the edge of its parent grid. This modified version of WRF is an update of the version used by *Tulich and Kiladis* [2012] to perform cloud-resolving simulations of convection in the tropics. In that study, the SST was highly peaked at the equator, and the background mean zonal winds were held fixed to isolate the effects of different wind shear profiles on the convective dynamics. In this study we use broader, more realistic SST profiles and the simulations are fully interactive so that realistic Hadley circulations can develop. An additional modification is that the position of the sun is fixed at a permanent equinox, with the diurnal cycle retained.

All simulations use an outer domain with either 139.05 km or 46.35 km resolution. The "aquachannel" refers to simulations with a single domain that is equal to the length of the equator in the zonal direction (e.g., 288 grid points at 139.05 km grid spacing) and with a meridional extent that is equivalent to the distance from 60S to 60N on the Earth (e.g., 96 grid points at 139.05 km). The boundary conditions are periodic in the zonal direction, with free-slip walls at the north and south boundaries. Additional simulations have the same meridional extent but are zonally one-third the length of the equator and use either 139.05 km grid

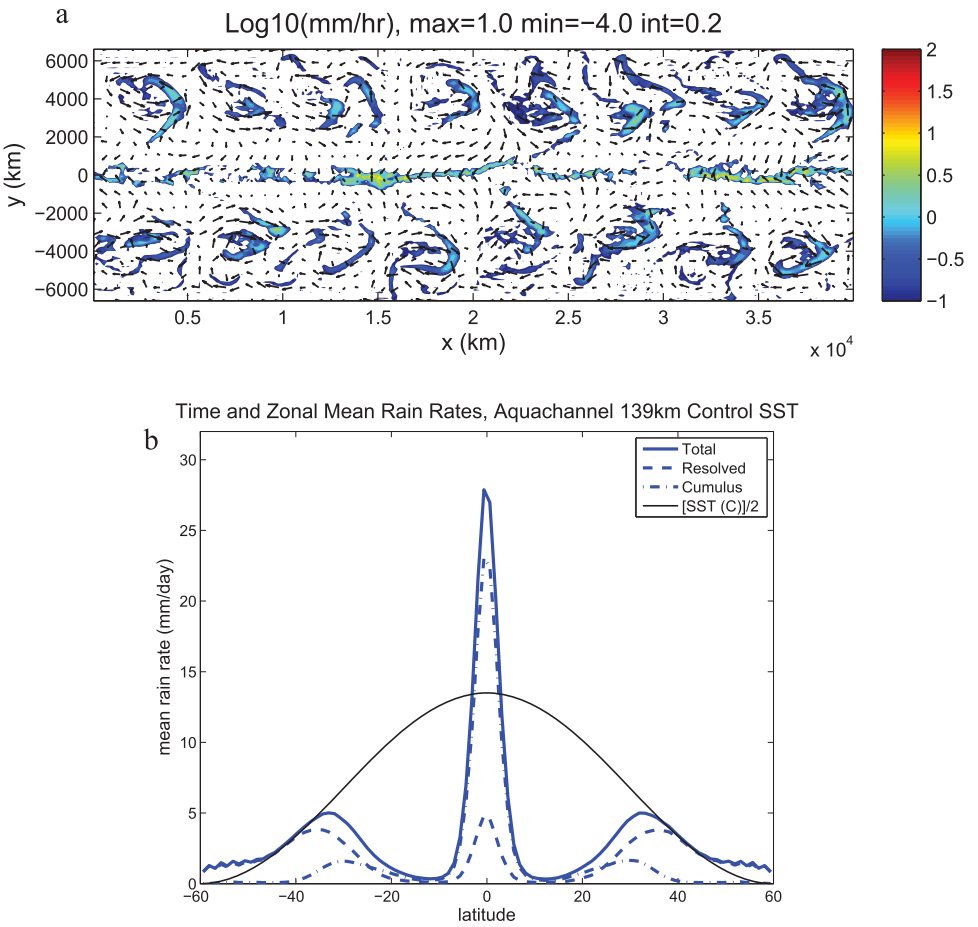

Figure 2. Precipitation distributions in the 139 km aquachannel simulation: (a) an example of instantaneous rain rate, shown in terms of the base 10 logarithm of the rain rate in mm h^{-1}, along with surface wind vectors; (b) time-zonal mean resolved and parameterized rain rates over year 2, in mm d^{-1}.

spacing (96 × 96 points) or 46.35 km grid spacing (288 × 288 points). This square domain is the "aquapatch." When nesting is used, grids with 1/3 the grid spacing of their parent domains are embedded in the outer domain. Nesting once from 46.35 km with a 3:1 grid ratio achieves a local grid spacing of 15.45 km; nesting again achieves 5.15 km spacing. These horizontal grid configurations are shown in Figure 1. For brevity, these resolutions will hereafter be referred to as 139 km, 46 km, 15 km, and 5 km.

All simulations use 50 levels in the vertical direction, with the model top reaching to approximately 26 km or approximately 24 hPa. The model levels were unevenly distributed in height to provide greater resolution in the boundary layer and around the tropopause, with 10 model levels between the surface and 1.2 km height, and 10 model levels between 12 and 18 km height.

We use the following parameterizations: the Goddard microphyics scheme [*Tao et al*., 2003], the Goddard shortwave and longwave radiation schemes [*Chou et al*., 1998; *Chou and Suarez*, 1999], and the YSU planetary boundary layer scheme [*Hong et al*., 2006]. The surface layer formulations coupled to the YSU scheme have been modified such that moisture fluxes as a function of wind speed are similar to the formulation of *Fairall et al*. [2003]. Most of the simulations use the modified Tiedtke cumulus scheme [*Tiedtke*, 1989; *Gregory et al*., 2000] as implemented in WRF version 3.4.1 [*Wang et al*., 2007].

At all points the surface is defined to be a ocean with fixed SST. We use two of the SST profiles proposed by *Neale and Hoskins* [2001] for the aquaplanet experiment (APE): the narrower "control" SST profile and the broader "observed" profile. Both the control and observed profiles are based on analytical functions of latitude. The observed profile is fairly close to the Earth's zonal mean SST after it has

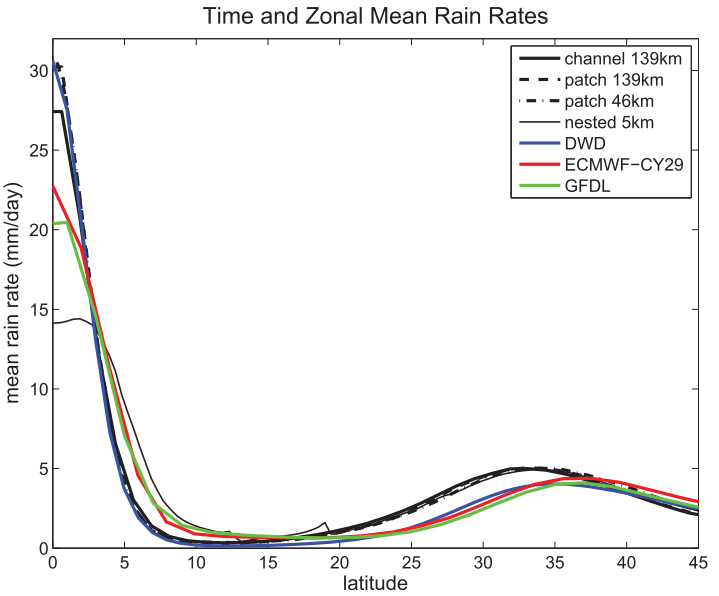

Figure 3. Time-zonal mean rain rates from year 2 of the aquachannel and aquapatch simulations (black curves) compared to three of the APE simulations.

been symmetrized about the equator. All simulations begin with the atmosphere at rest using a tropical sounding.

Finally, the Coriolis parameter is defined using the beta-plane approximation $f = \beta y$, with $\beta = 1.6 \times 10^{-11}$ m^{-1}s^{-1} as for the real Earth. Extending this formulation from the equator to the midlatitudes is unquestionably a poor approximation to the geometry of a spherical planet. $f = 2\Omega\sin(\phi)$, where ϕ is latitude, can also be used in WRF, as in *Nolan et al.* [2010], but that is also a somewhat unphysical configuration. Despite the unusual geometry and the β-plane approximation, we will show in section 3 that the resulting wind, temperature, and precipitation fields in the tropics are very similar to those generated from spherical models, and the mean flows and eddies in the midlatitudes are also quite similar.

3. The Aquachannel and the Aquapatch

3.1. Aquachannel Results and Validation

We begin with the full-length aquachannel using 139 km grid spacing. The domain size is 288 × 96 grid points. The control SST profile is used. The simulation is integrated for 2 years and statistics are computed over the second year.

Figure 2a shows a snapshot of instantaneous rain rate and surface wind vectors. The basic features of the general circulation are evident: an ITCZ exists along the equator where northeasterly and southeasterly winds converge. A series of baroclinic waves, some with attendant fronts, march across the midlatitudes. Inspection of numerous output times revealed that there are almost always 8 such waves, occasionally 9, in various stages of development (not shown). Near the northern and southern boundaries, the mean surface flow reverses again to easterly; on aquaplanets this happens near the poles. The precipitation in the ITCZ is zonally concentrated in two distinct regions along the equator. These mark the locations of convectively coupled Kelvin waves (CCKWs) that will be discussed later.

The time and zonal mean rain rates are shown in Figure 2b. The total rain rate peaks near 30 mm d^{-1} at the equator, decreases to less than 1 mm d^{-1} in the subtropics, and then peaks again at almost 5 mm d^{-1} near the 35° latitude. About 80% of the rain in the tropics is from CP, whereas poleward of 40S/N, virtually all the precipitation is explicitly generated. Note that here "latitude" refers to an equivalent distance from the equator, i.e., 111 km per degree.

Using the APE simulations as reference, the total rain rate distribution is very similar to the rain rates produced by many of the spherical aquaplanets. Figure 3 compares the aquachannel time-zonal mean rain rate to three of the APE cases: the Geophysical Fluid Dynamics Laboratory (GFDL) model, the European Centre for Medium-range Weather Forecasting (ECMWF) model (version CY29), and the German Weather Service (DWD) model. Details about these models and the specific versions of each are provided in Tables 2–4 of B13. Relative to all of the APE models, the DWD model configuration was the most similar to the aquachannel, in that it used the Tiedtke cumulus scheme (as implemented in that model) and the grid spacing was about 1°. Not surprisingly then, its equatorial rain rate is very similar to the aquachannel, around 30 mm d^{-1}, decreasing to less than 1 mm d^{-1} in the range of 10–20° latitude.

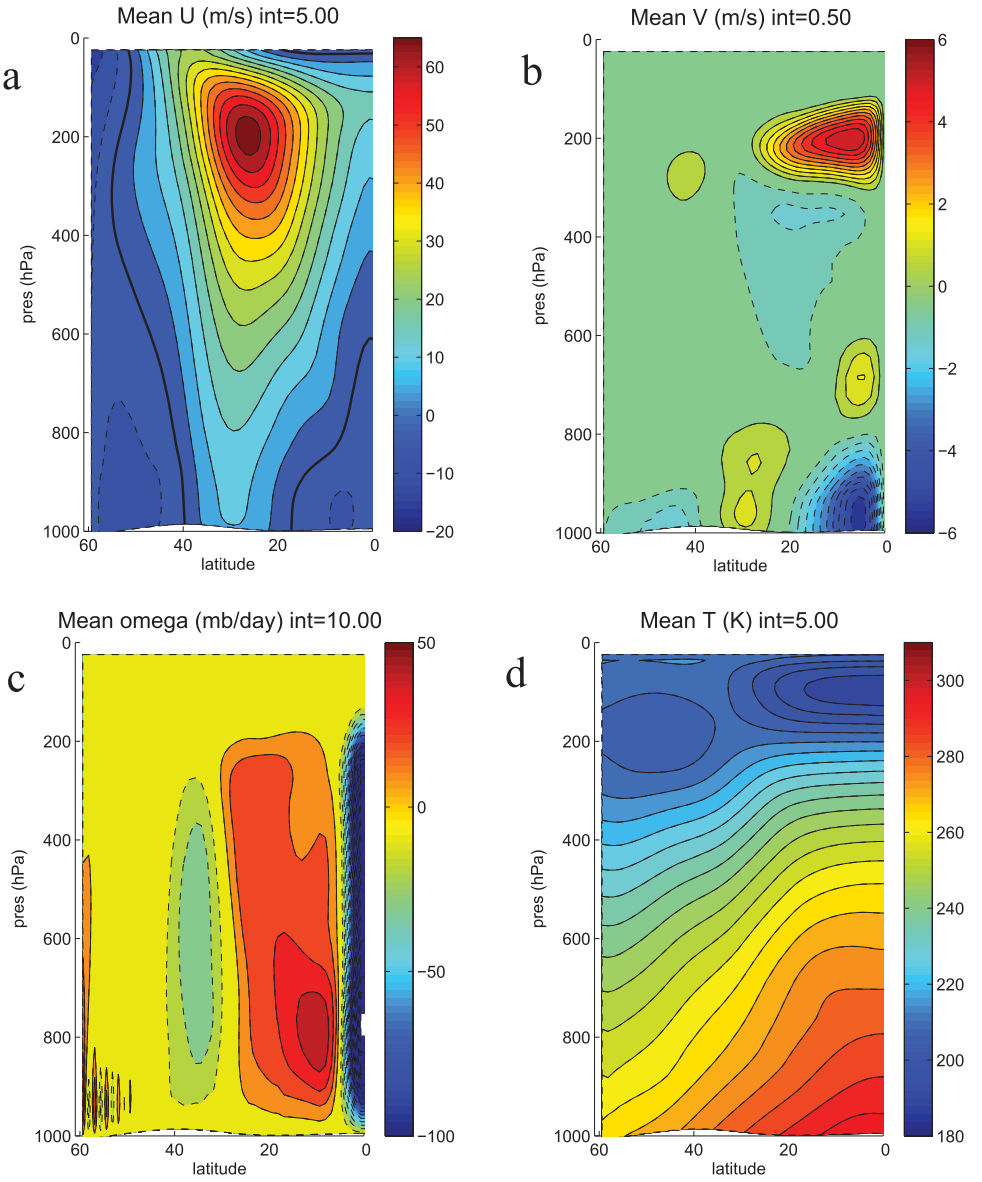

Figure 4. Time-zonal mean fields from 1 year of model output for the aquachannel simulation using the control SST profile: (a) zonal wind, (b) meridional wind, (c) vertical wind in pressure coordinates, (d) temperature. The zero contour is included as a thick line in Figure 4a.

Figure 4 shows time-zonal mean fields of zonal, meridional, and vertical winds, and temperature as functions of latitude and pressure. The plots are designed to be easily compared to time-zonal means from the APE simulations shown in B13, W13, and the ATLAS, such as the multimodel means shown Figure 3 of B13. Since it is not the result of an average over many models, the mean general circulation of the aquachannel shows much sharper features, most notably in the meridonal (v) and vertical (w) winds, but otherwise it is structurally very similar to the APE multimodel mean. Water vapor (q_v) and relative humidity (RH) are also very similar (not shown). There are a few consistent differences between the aquachannel and APE results. The most obvious is that the Hadley cell and its associated structures are narrower in the aquachannel. For example, the zonal jet peaks at about 26 S/N in the aquachannel, as compared to locations ranging from 28 to 30 S/N in most of the APE simulations.

A more explicit comparison of the zonal wind profiles is shown in Figure 5a. Along with the equatorward shift of the mean jets, it is evident that, in contrast to the APE models chosen for comparison, the aquachannel has significant upper-level super-rotation, i.e., upper-level westerlies at the equator. As can be seen from Figure 4a, westerly winds at the equator are maximized around 100 hPa and extend downward

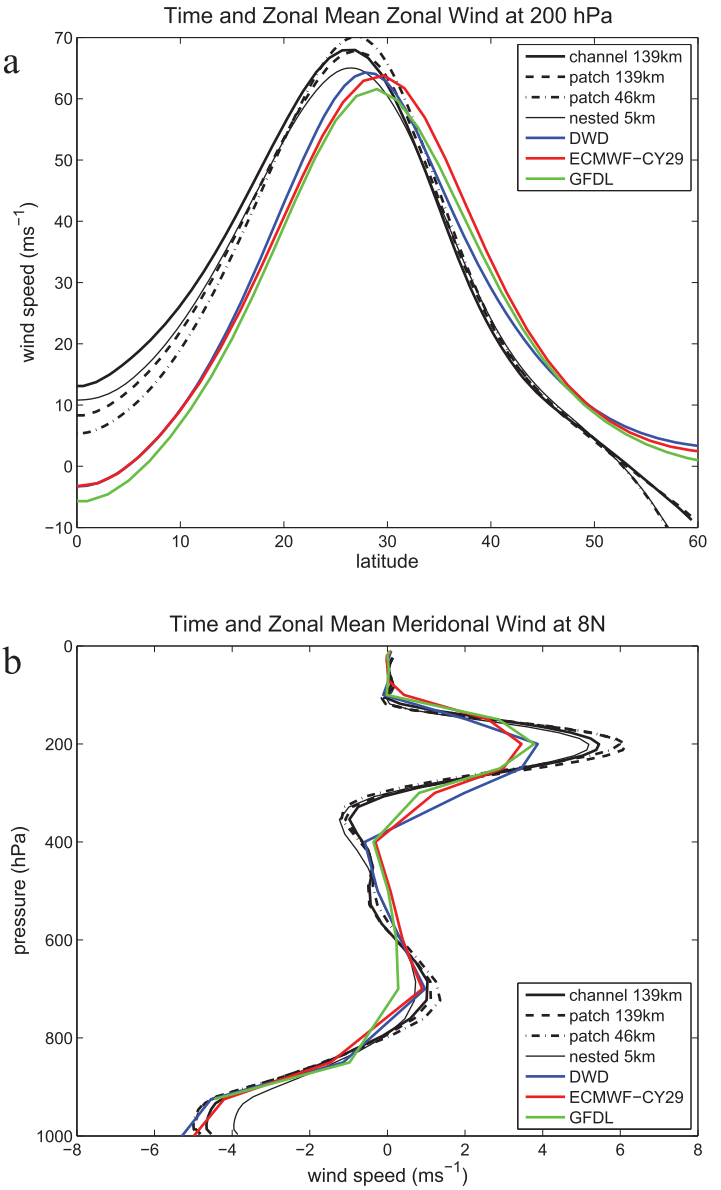

Figure 5. Profiles of (a) zonal wind at 200 hPa height, and (b) meridional wind at latitude 8°N, for the various aquachannel and APE simulations.

considerably, changing to easterly winds below 600 hPa. Some of the other APE simulations also show equatorial westerlies at 200 hPa, such as the LASG and MRI models (see Figure 4.17 of the ATLAS), but none of them have westerly winds over such a deep layer.

After most of the simulations for this study were completed, some additional tests were performed using $f = 2\Omega\sin(\phi)$. These simulations produced zonal jets that were closer to, although still not quite equal to, the jet locations of the aquaplanets. The more realistic variation of f also diminished the superrotation at the equator, with the mean zonal winds at 200 hPa in the aquachannel being reduced from about 13 ms^{-1} to 9 ms^{-1}.

Vertical profiles of the meridional wind v at 8N are shown in Figure 5b. All simulations show the four flows in and out of the ITCZ discussed by *Nolan et al.* [2010]: the boundary layer inflow, the shallow return flow, the midlevel inflow, and the upper-level outflow. The strengths and depths of the boundary layer inflow and the shallow return flow for the aquachannel are very similar to those of the three APE simulations. The aquachannel has a more pronounced midlevel inflow and a substantially stronger upper level outflow jet. The stronger outflow jet appears to be due to the increased mass flux into the ITCZ associated with the mid-level inflow (which is nearly nonexistent in the APE profiles), and the narrower vertical extent of the outflow . Both of these, in turn, are likely due to the greater vertical resolution in our model.

A higher order validation of the aquachannel climate can be seen by comparisons to mean eddy fluxes. Figure 6 shows the variance and fluxes associated with transient eddies (specifically, $\overline{[v'^*2]}$, $\overline{[u'^*v'^*]}$, $\overline{[v'^*T'^*]}$, and $\overline{[v'q_{tot}{}'^*]}$, where q_{tot} is the total water including condensate, bars indicate time means, brackets indicate zonal means, and primes and stars indicate deviations from each, respectively). These plots can be compared to some of the plots in Figure 6 of B13. The structures of the heat and moisture fluxes in the aquachannel are quite similar to the APE multimodel means, and they are especially similar to those of the DWD model (see Figure 4.59 of the ATLAS). $\overline{[v'^*2]}$ in the aquachannel shows a more intricate structure than in any of the APE results, with its maximum considerably weaker but also more narrowly localized in the vertical, perhaps again due to the greater vertical resolution.

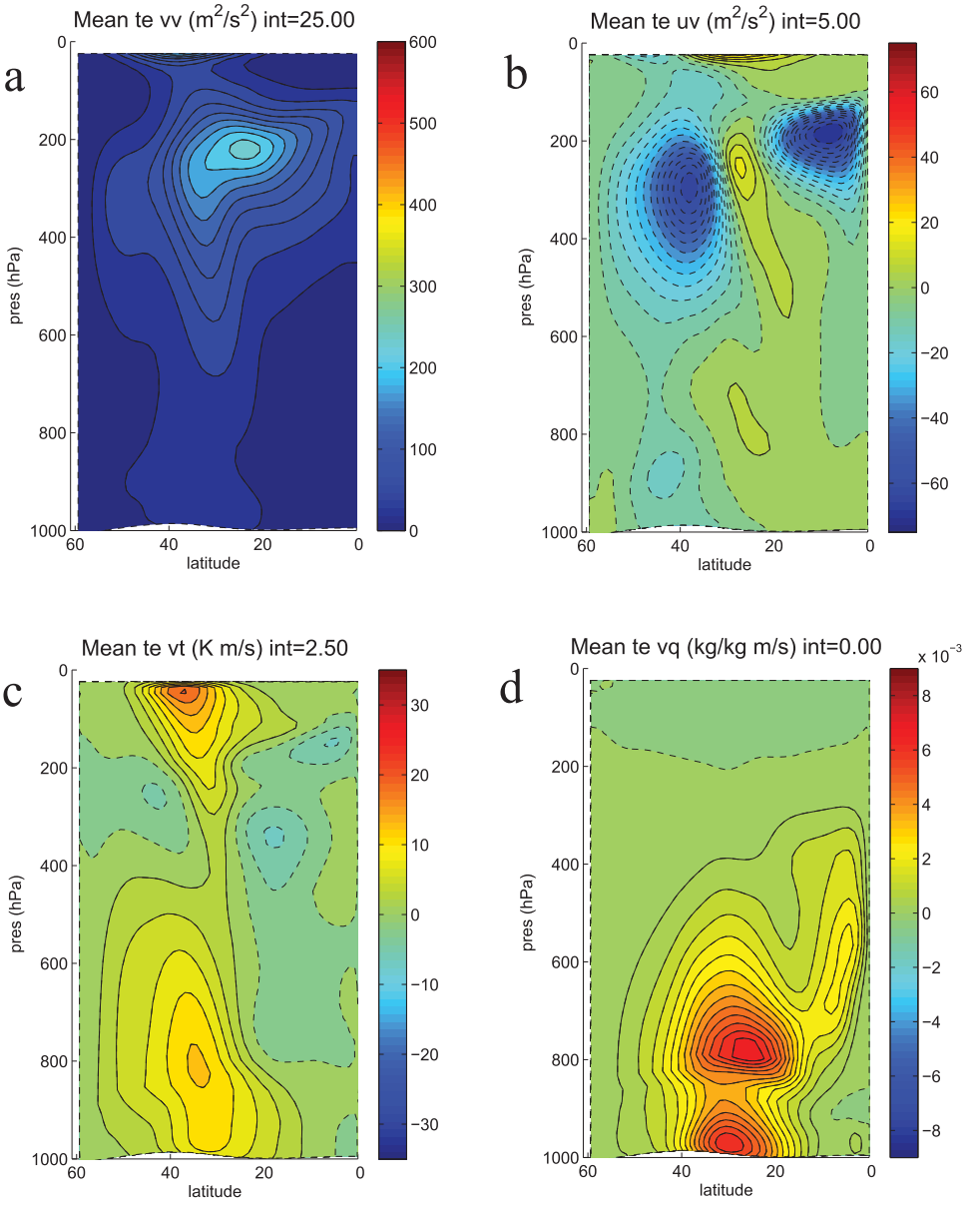

Figure 6. Time-zonal mean fields for some covariances of the transient mean eddies for the aquachannel with the control SST profile: (a) $\overline{[v'^{*2}]}$, b) $\overline{[u'^{*}v'^{*}]}$, c) $\overline{[v'^{*}T'^{*}]}$, and d) $\overline{[v'q_{tot}{}'^{*}]}$.

Of the four fluxes, the eddy momentum flux $\overline{[u'^{*}v'^{*}]}$ shows the largest deviation from the APE models. Perhaps this should not be surprising, since it is eddy fluxes of momentum (or rather, angular momentum) that are most sensitive to the unusual geometry of the aquachannel. Figure 7 shows meridional profiles of the eddy fluxes at 200 hPa for the aquachannel and the APE cases. The aquachannel eddy momentum fluxes are substantially more equatorward than for the aquaplanets, most notably near the equator, which helps to explain the increased westerly winds there. The eddy transports of heat and moisture are also significantly less in the aquachannel than the aquaplanets. A good part of this difference can be explained simply by geometry: the zonal length of the aquachannel does not change with increasing latitude, while the aquaplanets become shorter. At 30N, the aquachannel is 15% longer than the aquaplanet; mean fluxes that are 15% less will transport the same net quantity poleward.

To summarize, the aquachannel with the control SST profile produces a very similar global climatology as comparable aquaplanet simulations, with the only notable difference being its significantly stronger westerly flows at upper levels in the tropics. The midlatitude eddy fluxes of heat, moisture, and momentum are

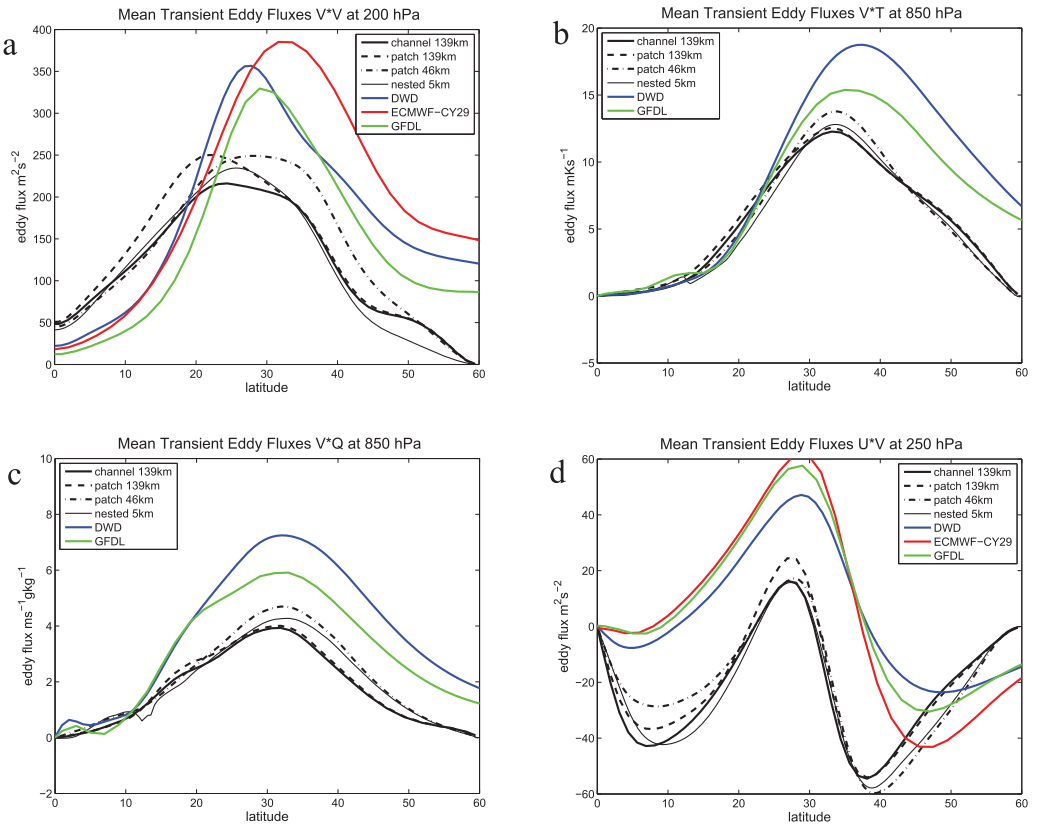

Figure 7. Profiles at 200 hPa of transient mean eddy fluxes for the various aquachannel and aquapatch simulations, and two of the APE simulations: (a) $[v'^{*2}]$, b) $[u'^{*}v'^{*}]$, c) $[v'^{*}T'^{*}]$, and d) $[v'q_{tot}{}'^{*}]$. Temperature and moisture fluxes that were available for the ECMWF model were erroneous and are not show.

all less in the aquachannel than in the aquaplanets, and these differences are consistent with the altered geometry of the aquachannel.

3.2. The Low-Resolution and High-Resolution Aquapatch

The next step is to take the 139 km resolution aquachannel and to shorten its length by a factor of 3, resulting in a square domain with each side having length equal to the distance from 60S to 60N on the earth. This is the aquapatch (Figure 1b). The simulation is repeated with 1 year spin-up time and means are computed for 1 year.

The mean general circulation in the 139 km aquapatch is very similar to that of the aquachannel. Due to its shorter length, two or three (as opposed to 8 or 9) baroclinic waves are almost always found on each side of the equator (not shown). The time-zonal mean rain rates and fields of *u*, *v*, *w*, and *T* are nearly identical to those of the aquachannel. Some explicit comparisons of the aquapatch and the aquachannel (and the aquaplanets) are available in Figures (3 and 5), and 7. Much of the commentary regarding the means and eddy fluxes that is applied above to the aquachannel also holds for the aquapatch, with the notable difference that the upper-level westerlies are not as strong in the aquapatch.

Next, the horizontal resolution of the aquapatch is tripled, changing the grid spacing to 46 km. Snapshots of the rain rate show the pattern of 3 or occasionally 2 baroclinic waves in each of the midlatitudes (Figure 8). The time-zonal mean total rain rate is also nearly identical, although now about half of the rain produced at the equator is from explicit precipitation.

If an aquapatch that is 1/3 the length of the Earth can produce nearly the same general circulation as the aquachannel, how much shorter can we go? Additional simulations were performed using 46 km resolution and channel lengths that are 2/3, 1/3, and 1/6 of the aquapatch (or 2/9, 1/9, and 1/18 of the Earth). Their rain rates and zonal wind profiles are shown in Figure 9. Remarkably, a very similar climatology to the

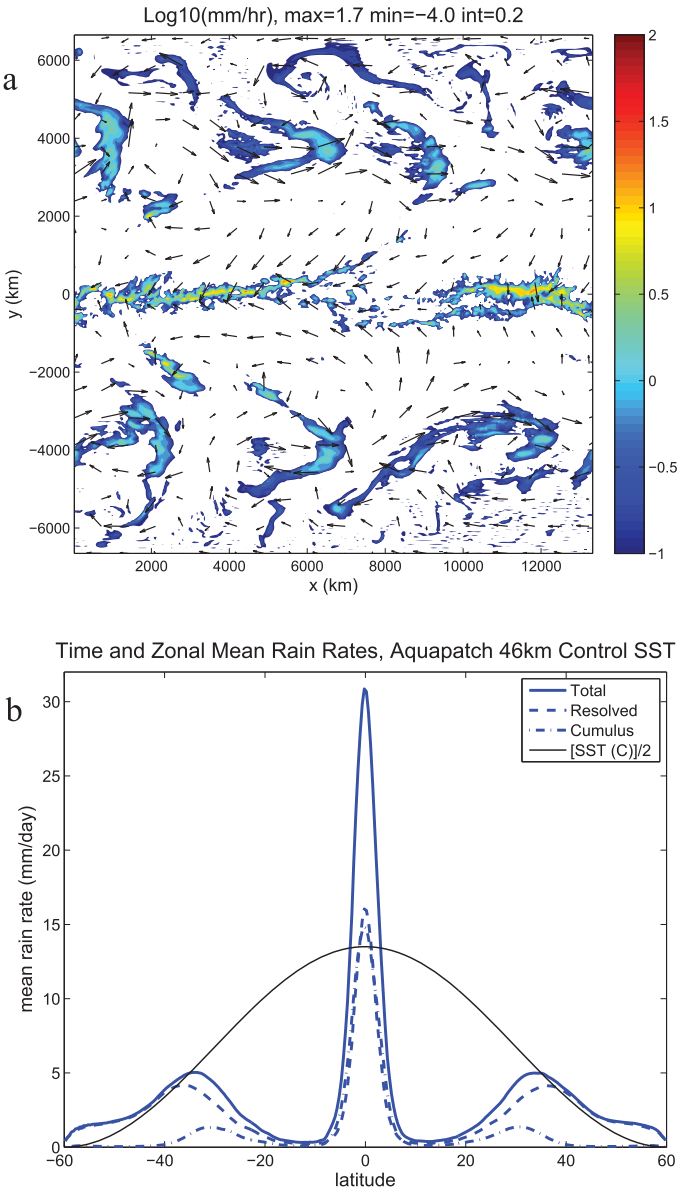

Figure 8. Precipitation fields for the aquapatch with 46 km resolution: (a) snapshot of instantaneous precipitation, and (b) time-zonal mean rain rates.

aquachannel (and the aquaplanets) can be reproduced with the 2/3 and 1/3 length aquapatches. In these cases, there is almost always either 2 or 1 baroclinic waves, respectively, on each side of the equator. Apparently the eddy transports of these waves are enough to ventilate the tropics and produce a climate similar to the aquaplanet. For the 1/3 aquapatch, the zonal wind profile at 200 hPa shows an exaggerated jet due to reduced angular momentum transports (not shown). The 1/6 aquapatch produces a drastically different climate, with a very strong and narrow ITCZ, virtually no rain in the subtropics, reduced rain rates in the midlatitudes, and an even more exaggerated subtropical jet. In fact, the time-zonal wind fields of the 1/6 aquapatch are reminiscent of axisymmetric simulations [e.g., *Schneider*, 1977; *Held and Hou*, 1980].

3.3. Convectively Coupled Waves

Within the ITCZ, the dominant precipitation features in the tropics for all simulations are convectively coupled Kelvin waves (CCKWs) [*Kiladis et al.*, 2009]. The snapshots of rain-rate in Figures 2a and 8a show precipitation in the ITCZ zonally concentrated in one or two regions. While the mean low-level wind is easterly and the individual convective cells move westward, these precipitation "super-clusters" move eastward with speeds of 15–20 ms^{-1}. Figure 10 shows Hovmöller diagrams of total precipitation averaged in the 5S to 5N band for the 139 km aquachannel and the 46 km aquapatch. Both diagrams show distinct eastward moving features, with weaker, smaller-scale, and slower westward moving features embedded within them. The mean CCKW phase speeds are 19.1 and 15.3 ms^{-1} for the aquachannel and the aquapatch, respectively. Some of this difference may be due to the significantly stronger upper-level westerlies (13 ms^{-1} versus 7 ms^{-1}) at the equator for the aquachannel versus the aquapatch (see Figure 12a).

Also shown are power-spectra using methodologies similar to those described in *Wheeler and Kiladis* [1999]. Note that the *x*-axis for the aquapatch simulation shows zonal wavenumbers 1 through 5, rather than 1 through 15, since wavenumber 5 in the aquapatch is equivalent in length scale to wavenumber 15 in the aquachannel.

These figures can be compared to similar Hovmöller diagrams from the APE papers, such as Figures 16 and 17 from B13 or Figure 4.93 of the ATLAS. The power spectra from the aquachannel and aquapatch are quite similar to those of the APE simulations, with particularly good agreement with the aforementioned DWD

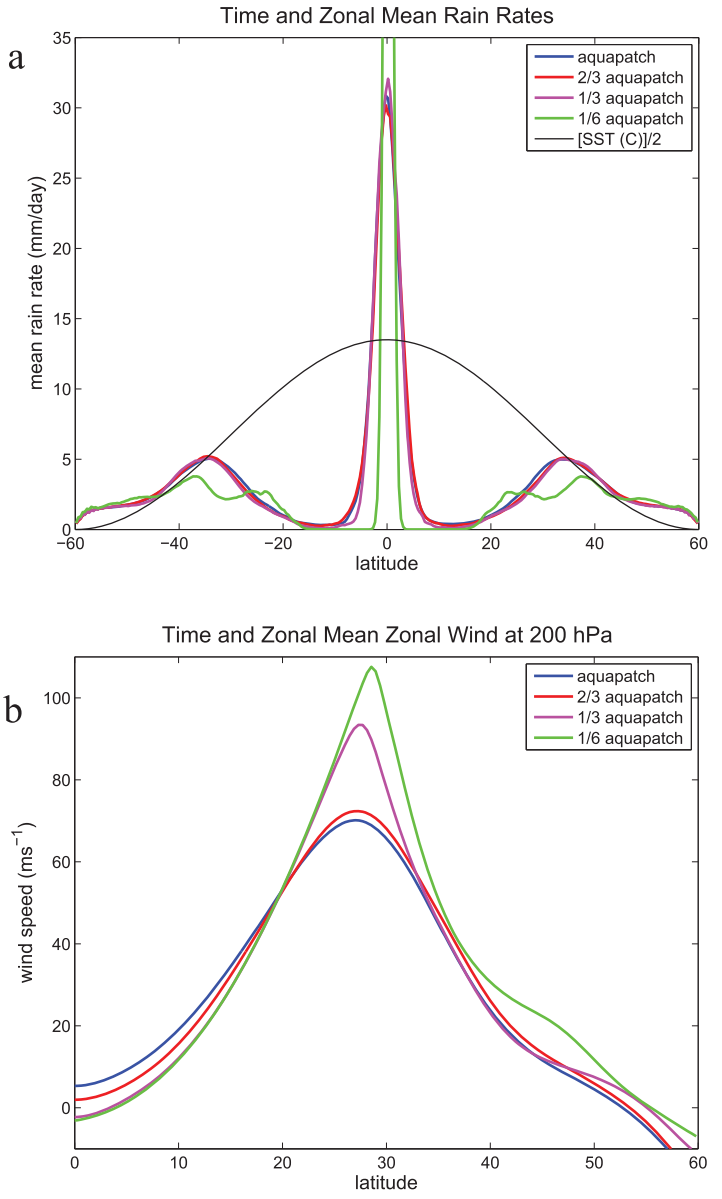

Figure 9. Time-zonal mean outcomes for aquapatch simulations with even shorter lengths in the zonal direction: (a) rain rate across the entire domain; (b) zonal wind at 200 hPa for positive latitudes.

model. A more complete analysis of the CCKWs in these simulations, including composite structures and comparisons between parameterized and resolved convection, will be the subject of a separate paper.

3.4. The Aquapatch With Nesting

To achieve a horizontal resolution that would be appropriate for not using CP, two nested grids are embedded in the high-resolution aquapatch. For the control case, the 15 km grid has 864 $\times$ 288 points, covering from 20.0S to 20.0N. The 5 km grid has 2592 $\times$ 576 grid points, covering from 13.3S to 13.3N. Both of these domain edges are well outside the high precipitation zone of the ITCZ for the control case. Due to their high computational costs, the nested simulations were only performed for 18 months. They used only domain 1 for the first 4 months, domains 1 and 2 for the next 4 months, and then all three domains for the next 10 months. The last 6 months were used for analysis.

Snapshots of the precipitation and wind fields for the 46 km domain and a subset of the 5 km domain are shown in Figure 11, along with the time-zonal mean rain rates. Using the 5 km grid without parameterization results in broader precipitation fields, both instantaneously and in the mean. Mean profiles of rain rate, winds, and eddy fluxes for the nested aquapatch case are included in Figures (3 and 5), and 7. The time-zonal mean fields are generally similar to the previous results, but are consistent with a broader and weaker ITCZ, generating a slightly weaker zonal jet. The reasons for the broader ITCZ will be discussed later in the paper.

Although it is hard to tell from the figures, the domain-averaged rain rates are very similar across all the simulations. For the 139 km aquachannel, the 139 km aquapatch, the 46 km aquapatch, and the 5 km nested aquapatch, these are 3.41, 3.45, 3.49, and 3.35 mm d^{-1}. The total precipitation nearly balances total evaporation, with the former being about 1% less than the latter for the three CP simulations, and 0.3% less for the nested 5 km simulation.

Another feature that is evident in Figure 11, unfortunately, is a local discontinuity in the rain rate on either side of the nesting interfaces, with narrowly confined increases in rain rate on the inside of each interface, each matched by a nearly equal decrease in rain rate on the outside. Interestingly, these jumps in rain rate

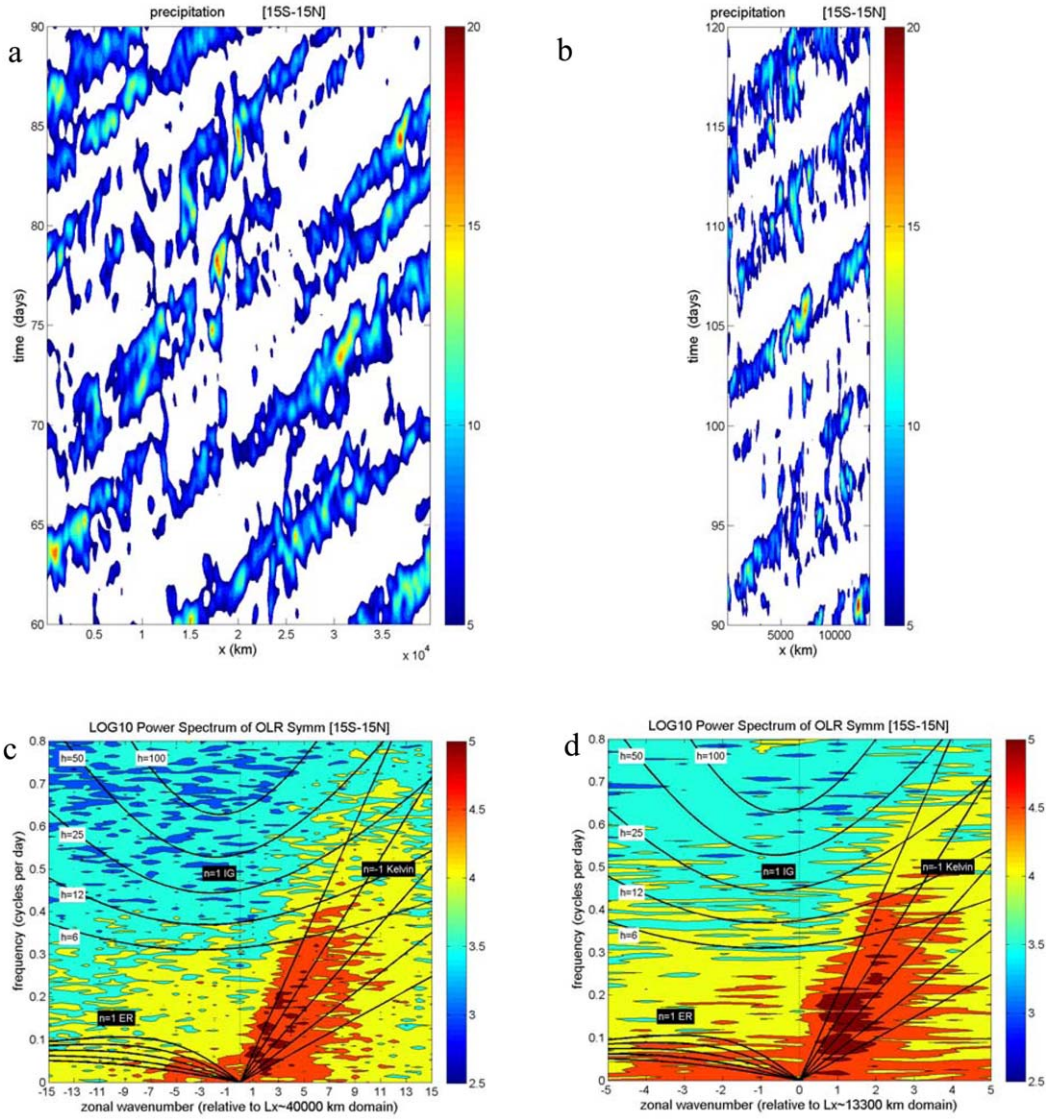

Figure 10. Hovmöller diagrams of total rain rate within 15° of the equator, in mm d^{-1}, for (a) the 139 km aquachannel and (b) the 46 km aquapatch, and Wheeler-Kiladis-style power spectra for symmetric outgoing longwave radiation within 15° of the equator, for (c) the 139 km aquachannel and (d) the 46 km aquapatch.

only occur in the explicit rain, as the parameterized rain rate varies smoothly across the interface from domain 1 to domain 2. Tests also found that this jump in explicit rain occurs whether or not the cumulus scheme is present in either or both domains. The discontinuity appears even when a nest interface is relocated well into the midlatitudes. One possible cause for the jump in rain rates on the higher resolution sides of each interface is that smaller grid spacing allows for smaller-scale updrafts, which for dynamical reasons can be stronger than wider updrafts [*Weisman et al*., 1997; *Pauluis and Garner*, 2006; *Morrison*, 2016].

It is natural to wonder how much of the differences in the rain-rate profile between the 46 km aquapatch and the 5 km nested simulations are due to the increased resolution and how much are due to the use (or not) of the CP. While the high computational cost of the 5 km simulations prohibits repeating it with CP active on all grids, this question can be answered to some extent by examining single-nest, 15 km simulations with and without CP, as shown in Figure 12. Both the decrease in grid spacing and the elimination of CP contribute to broadening of the rain rate distribution around the equator. The resolution effect from 46 km to 15 km is opposite to the change from 139 km to 46 km, which caused the rain rate to be more focused. However, for the 15 km case with CP, about 80% of the rain around the equator is already from

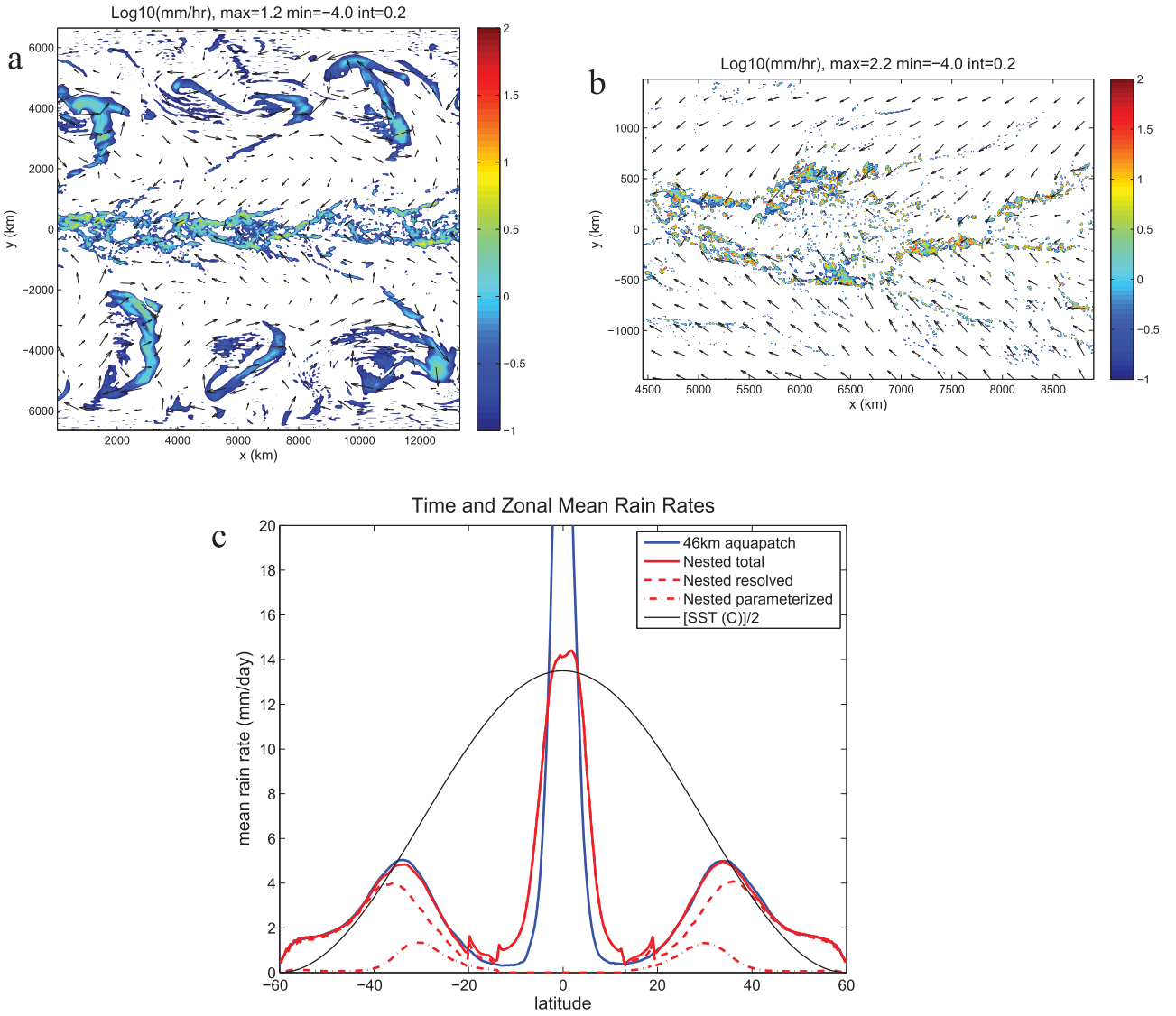

Figure 11. Results for the nested 5 km simulation with control SST profile: (a) snapshot of log10(rain rate) on the 46 km domain; (b) snapshot of log10(rain rate) from the 5 km grid, restricted to the middle 1/3 of the domain; (c) time and zonal mean rain rates, with comparison to the 46 km results. Note the full range of the blue curve in Figure 11c is shown in Figure 8b.

resolved processes, so that the processes by which higher resolution leads to a broader distribution (to be discussed below) are probably the dominant effect. *Bretherton and Khairoutdinov* [2015] used 4 km grid spacing in their aquachannel simulation, but also performed an additional simulation with 20 km spacing (without CP). The differences in rain rate profiles for their 4 km and 20 km results (see their Figure 17) are quite similar to those of the 5 km and 15 km simulations shown here. Bretherton and Khairoutdinov used the observed SST profile, but in the section 3.5we find similar changes using that profile as well.

3.5. Results for the "Observed" SST Profile

All simulations described in the previous sections were repeated for the *Neale and Hoskins* [2001] "observed" SST profile. To handle broader rainfall distributions, the boundaries of the 15 km and 5 km nested domains were extended to 30.0S/N and 20.0S/N, respectively.

Much like in many aquaplanet simulations (B13), this broader SST profile generates a more diverse set of rain rate distributions, as shown in Figure 13. Like the DWD model, the 139 km aquachannel simulation retains a single ITCZ and a general circulation very similar to that of the control profile. However, increasing to 46 km resolution changes the distribution to a distinctly double-ITCZ pattern, which it shares with the

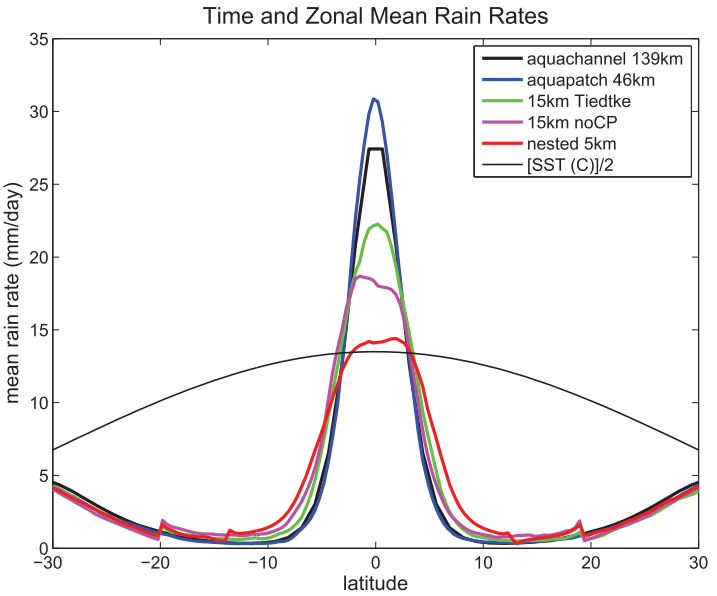

Figure 12. Time-zonal mean rain-rates for simulations nested to 15 km resolution, with and without the Tietdke cumulus parameterization activated.

ECMWF and GFDL simulations. In the aquapatch nested to 5 km, however, the rain rate distribution again becomes broader, and the rain rate at the equator becomes high enough to nearly eliminate the double-ITCZ pattern. This can also be seen in Figure 14, which shows that even without CP at 15 km, the change in the rain-rate profile between 15 km and 5 km is quite substantial.

As with the control SST, we can conclude that the tropical rain rates and general circulation patterns generated in the aquachannel and aquapatch simulations are reasonably similar to those of equivalent simulations on the sphere. A more interesting result, worthy of further study, is that using 5 km resolution without CP in the tropics leads to broader, more diffuse rain rate distributions in both cases, with the near-elimination of the double ITCZ pattern for the observed SST profile.

4. Simulated ITCZ Structure and the Convective Response to Atmospheric Forcing

4.1. Relationships Between Precipitation Rates and Atmospheric Parameters

We now focus on the result that the 5 km simulation without CP produces a broader rain rate distribution (Figure 11). A similar pattern, though less pronounced, was seen in the comparison of 15 km simulations with and without CP (Figure 12). Alternatively, one may wonder why the CP focuses precipitation into narrower bands, either on or off the equator.

To answer this question, first we attempt to determine exactly how rain rate depends on the local environment for the two different frameworks of moderate resolution with CP versus high resolution without CP. Of course, the rain rate production of a particular CP is determined by its assumptions, formulation, and programming. Unfortunately, the very strong nonlinearities built into most CP schemes makes predicting their rain rates from environmental variables *a priori* rather difficult. Instead, we will take the *a posteriori* approach of recording rain rates in the model output and correlating them with local environmental variables.

We sample rain rates in the ITCZ and its fringes every 6 h for 2 months. Only every 4th grid point in each direction is sampled. At each point, we also compute variables that are generally believed to be important for precipitation: surface evaporation (QFX), column relative humidity (CRH), boundary layer (0–1 km) moisture convergence (BLMC), and convective available potential energy (CAPE). The values of rain rate and each of these environmental variables are divided into 10 equally spaced bins, and joint frequency diagrams are constructed between rain rate and each of the variables.

As a first example, we consider the 46 km aquapatch with the control SST profile. The frequencies of each rain rate as a function of each of the aforementioned parameters is shown in Figure 15a. Each plot of the figure shows the number of times that the combined rates of resolved and parameterized rain (total rain, hereafter TR) was in the range indicated on the *y* axis when one of the environmental variables was in the range indicated on the *x* axis. Since zero and very small rain rates were extremely common, with frequencies typically 10 times or more greater than the higher rain rates, the lowest row of data corresponding to rain rates from 0 to 1.0 mm h^{-1} are not shown. For example, Figure 15a (top-left) shows that by far the most frequent occurrence (for rain rates $>$ 1.0 mm h^{-1}) was 1–2 mm h^{-1} when QFX was around 5×10^{-5} kg s^{-1} m^{-2}. Higher rain rates also occurred most frequently for the same evaporation rates. The other plots

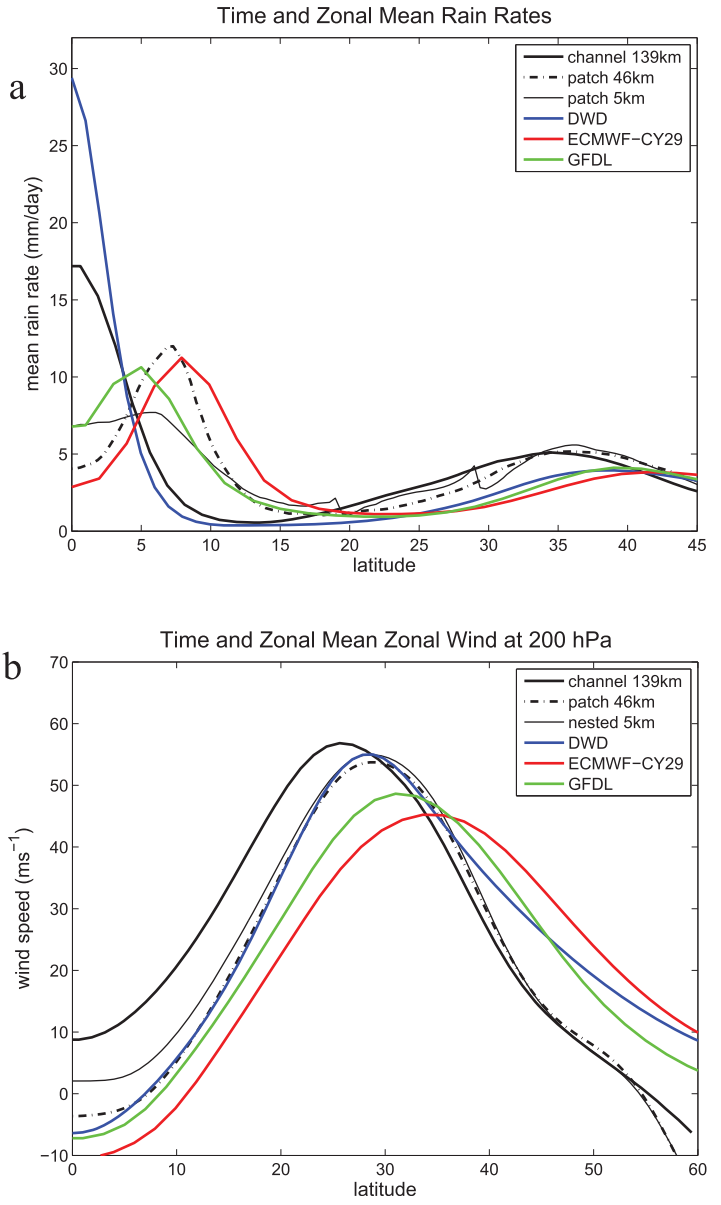

Figure 13. Results for simulations using the *Neale and Hoskins* [2001a] "observed" SST profile, with comparisons to some of the aquaplanet simulations: (a) mean rain rate; (b) mean zonal wind at 200 hPa.

show that rain rates of all values were most common when CAPE was around 1700 Jkg^{-1}, column RH was near 78%, and the boundary layer moisture convergence was around 1×10^{-7} kgs^{-1}m^{-2}.

This figure, however, is misleading. After all, why would not higher rain rates occur more frequently for higher values of CAPE? Why does the frequency drop off as CRH approaches its largest values? To identify what conditions are most favorable for a particular event, we have to normalize by how often each of those conditions occurs. This is achieved simply by dividing the frequencies in each joint bin by the total number of frequencies in each vertical column (including the large numbers of events for rain rates < 1 mm h^{-1}).

These normalized frequencies for the same simulation are shown in Figure 15b. The areas in white indicate that there were less than 100 events for the environmental predictor. For QFX, the normalized frequencies are slightly different, with the largest rain rates shifted toward slightly lower evaporation rates. This may indicate that where rain is falling, the boundary layer is already moistened, reducing evaporation. The normalized frequency distribution for CAPE indicates a preference for higher values of CAPE, with the frequencies of the highest rain rates peaking around 2000 Jkg^{-1}. Extrapolation of the values to the right would suggest that higher values of CAPE also produce significant rain, but there is insufficient data in that region. For CRH, the normalized frequencies show that, not surprisingly, its highest values are strongly correlated with the highest rain rates, with moderate rain becoming even more frequent than light rain when CRH $> 80\%$. The large increase in TR with CRH, shown more explicitly below, is consistent both with observations [*Bretherton et al.*, 2004; *Peters and Neelin*, 2006; *Holloway and Neelin*, 2009] and other simulations [*Tompkins*, 2001; *Grabowski*, 2003; *Derbyshire et al.*, 2004].

Normalized frequencies for BLMC are the most strikingly different, with two maxima, one for large positive values, and one for smaller negative values. In the raw frequency diagram (Figure 15a), the correlation between high rains rates and small values of BLMC is due to the generally positive values of BLMC that are occurring in and around the ITCZ, where rain most frequently occurs. However, the normalized frequencies show almost the opposite pattern, with strong correlations between high rain rates and both positive *and*

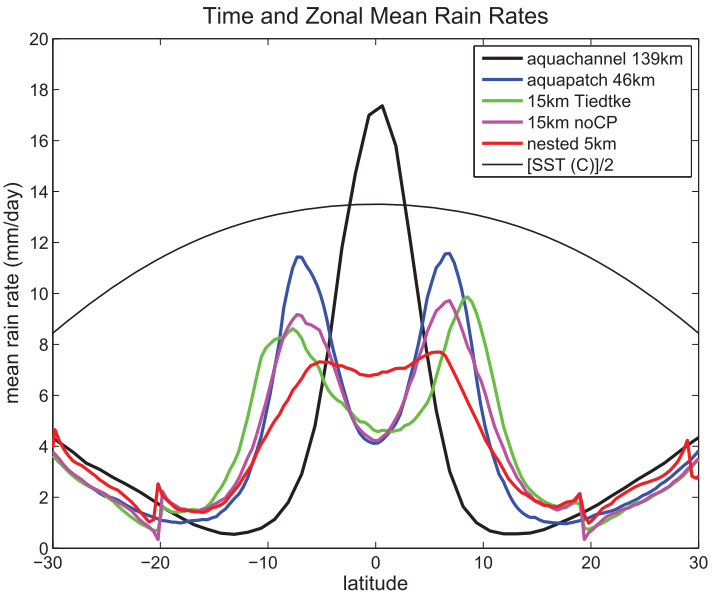

Figure 14. As in Figure 12, but for the observed SST profile.

negative BLMC. Our hypothesis is that the first correlation is due to the convergence that occurs underneath deep convection, while the latter represents areas of stratiform precipitation that follow deep convective events.

Figurew 16a and 16b show the normalized frequencies for rain rates separated into convectively parameterized rain (CR) and explict rain (ER). The ER frequencies are generally lower, and show an even greater correlation with nearly saturated columns. For BLMC, ER shows the highest values for negative BLMC, while high values of CR are most correlated with positive BLMC. This supports our hypothesis that BLMC is most closely associated with deep convection, which eventually transitions to stratiform, where the evaporation of falling rain causes low-level cooling, sinking, and divergence (negative BLMC).

We would like to think of these diagrams of normalized frequency of TR as a symbolic representation of the rainfall production by a particular model framework. By "framework" we mean here the combined CP, microphysics scheme, and grid resolution. If this is the case, then we would expect that 1) the same model framework would produce similar diagrams for different environments, and 2) different frameworks would produce diagrams with notable differences. Figures 16c and 16d show the normalized frequencies for TR and ER for the 46 km aquapatch simulation with the observed SST profile, which produces a very robust double ITCZ. The ER rates are significantly reduced, and the CR rates are nearly identical to TR, and thus are not shown. Comparing Figures 15b and 16c, we can see that the TR frequencies for the control and observed SST simulations are quite similar, supporting point (1) above.

To support point (2) above, some normalized frequency diagrams for different cumulus schemes are shown in the Appendix A.

Our goal here is to understand the differences between moderate resolution simulations with CP and the high-resolution simulations without CP. Frequency diagrams for TR (equal to ER) for the 5 km nested aquapatch simulations with the control and observed SST profiles are shown in Figure 17. For a fair comparison to the previous results, these diagrams are generated from the model output on the 46 km grid (domain 1), which are simply the block-averaged values from the 5 km grid cells. These plots are generally similar to those above, but there are two important differences. First, the rain rates in the nested cases show much less preference for high CAPE. Significant rains occur without significant atmospheric instability. The same result was found for other measures of instability, such as boundary-layer moist static energy, or its difference between the surface and 600 hPa (not shown). Second, the 5 km rain rate frequencies are actually greater for moderate and low values of CRH than for the simulations with CP. Similar results were found for midlevel (500–700 hPa) humidity (not shown).

These diagrams suggest that the reason for the double ITCZ precipitation structure for the 46 km simulations using the observed SST profile and the Tiedtke scheme is that, in comparison to 5 km simulations without CP, the CP is actually produces too little rain in areas of moderate instability or moderate atmospheric moisture. This indicates that the positive feedbacks that cause convection to be localized or "aggregated" in the tropics - such as free-tropospheric moisture, boundary layer convergence, and reduced longwave cooling - are actually too strong. The 5 km simulations indicate there should be more rain in the fringes of the ITCZ, and also more rain at the equator when the SST profile is flatter there.

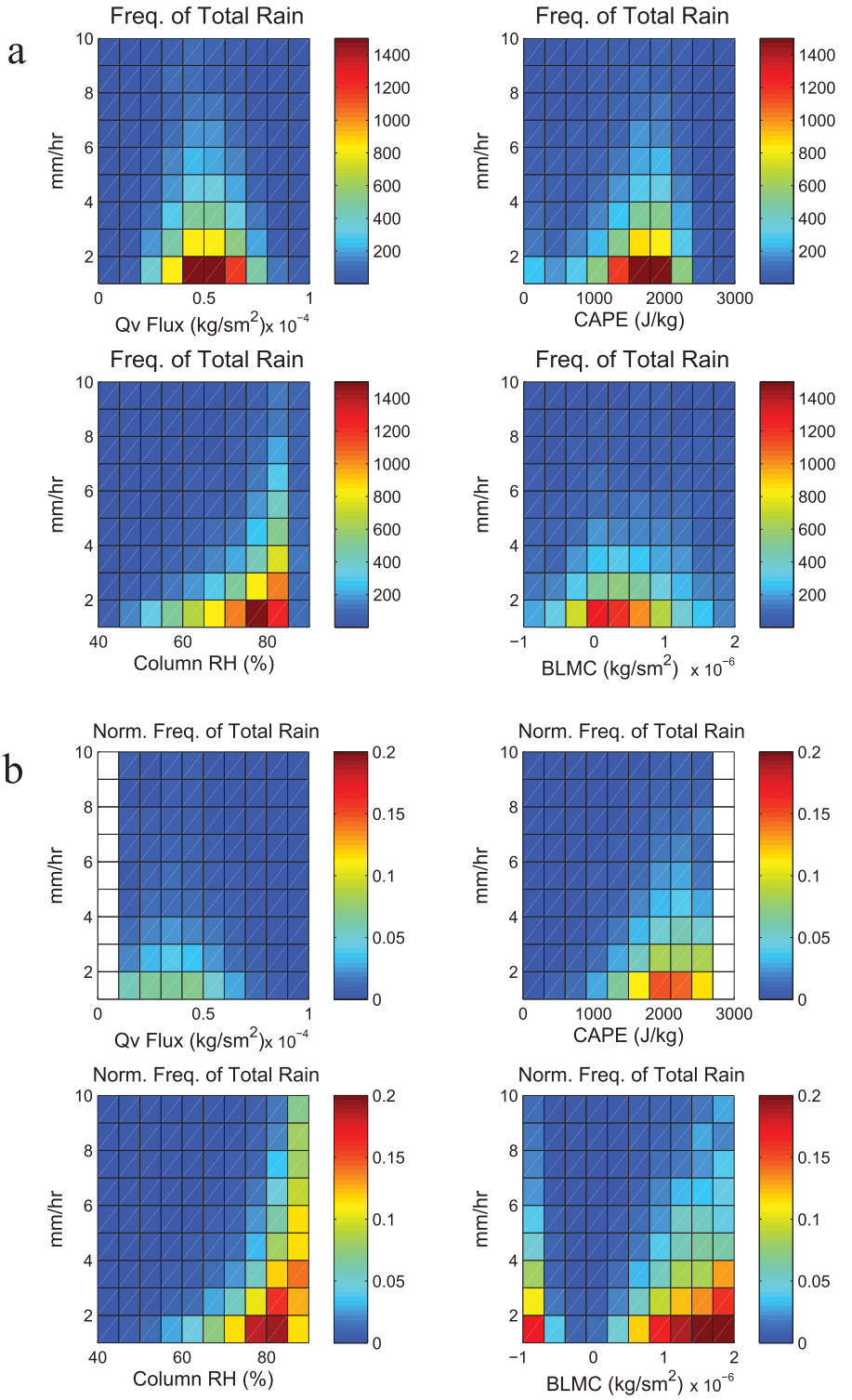

Figure 15. (a) Raw frequencies and (b) normalized frequencies for total rain rate as a function of various environmental variables in the 46 km aquapatch simulation with control SST profile. White squares indicate insufficient data.

A more condensed, and easier to compare, summary of these results is shown in Figure 17c, which conveys average TR as a function of each parameter, for the 46 km simulations with CP (blue curves) and the 5 km nested simulations (red curves). The differences at low values of CRH are easier to see, with 5 km resolution producing significantly greater mean rain rates at low CRH. It can be seen that for 5 km the mean rain rates

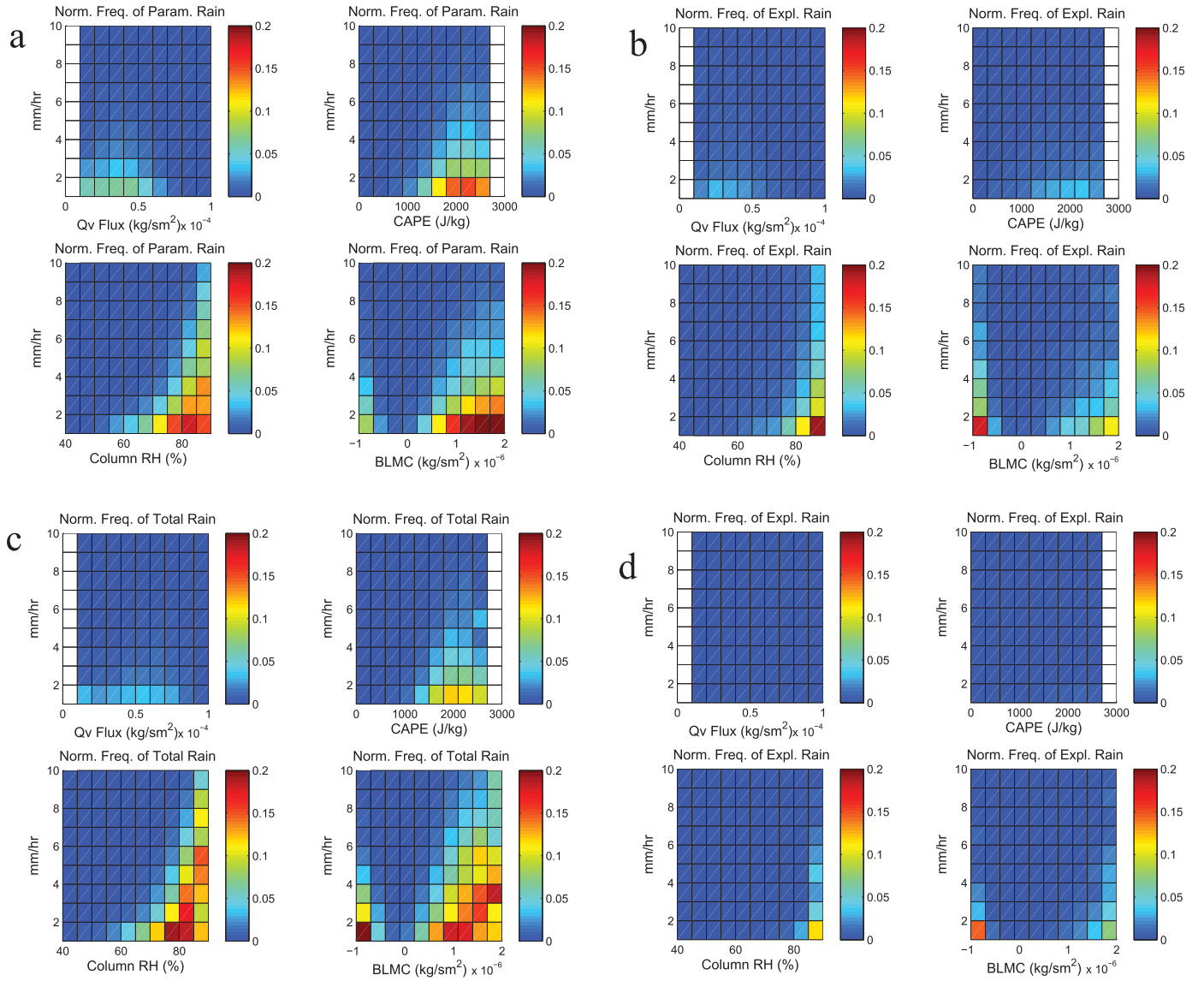

Figure 16. Normalized frequency diagrams for tropical rain rate versus environmental parameters for the 46 km aquapatch simulations: (a) control SST, parameterized rain; (b) control SST, explicit rain; (c) observed SST, total rain; (d) observed SST, explicit rain.

in the stratiform regions (associated with negative BLMC) actually produce more rain (on average) than the convecting regions.

4.2. Explicit Convection, Squall Lines, and Cold Pools

Consistent with many previous studies, we have found that simulations with CP tend to focus convection into narrow bands, either on the equator or in the double-ITCZ configuration [e.g., *Liu et al*., 2010; *Möbis and Stevens*, 2012]. The 5 km simulations without CP show either a single ITCZ or a very marginal double ITCZ, but more importantly, in both cases the rainfall distribution is broader, with lighter mean rain rates extending farther away from the equator or "filling in" the gap between the two off-equatorial maxima. Substantial rain occurs in these fringe regions despite reduced values of CAPE and CRH.

We propose that a significant reason for these differences in rainfall distributions and environmental sensitivities is because the 5 km simulations produce propagating squall lines and strong surface cold pools. Examination of numerous precipitation fields and animations reveals that, in the 5 km nested simulations, squall lines and other organized areas of convection tend to move meridionally away from the ITCZ. A few such bands can be seen in Figure 11b, such as from $x = 4500$ to 5500 km, along $y = 300$ km. In that case,

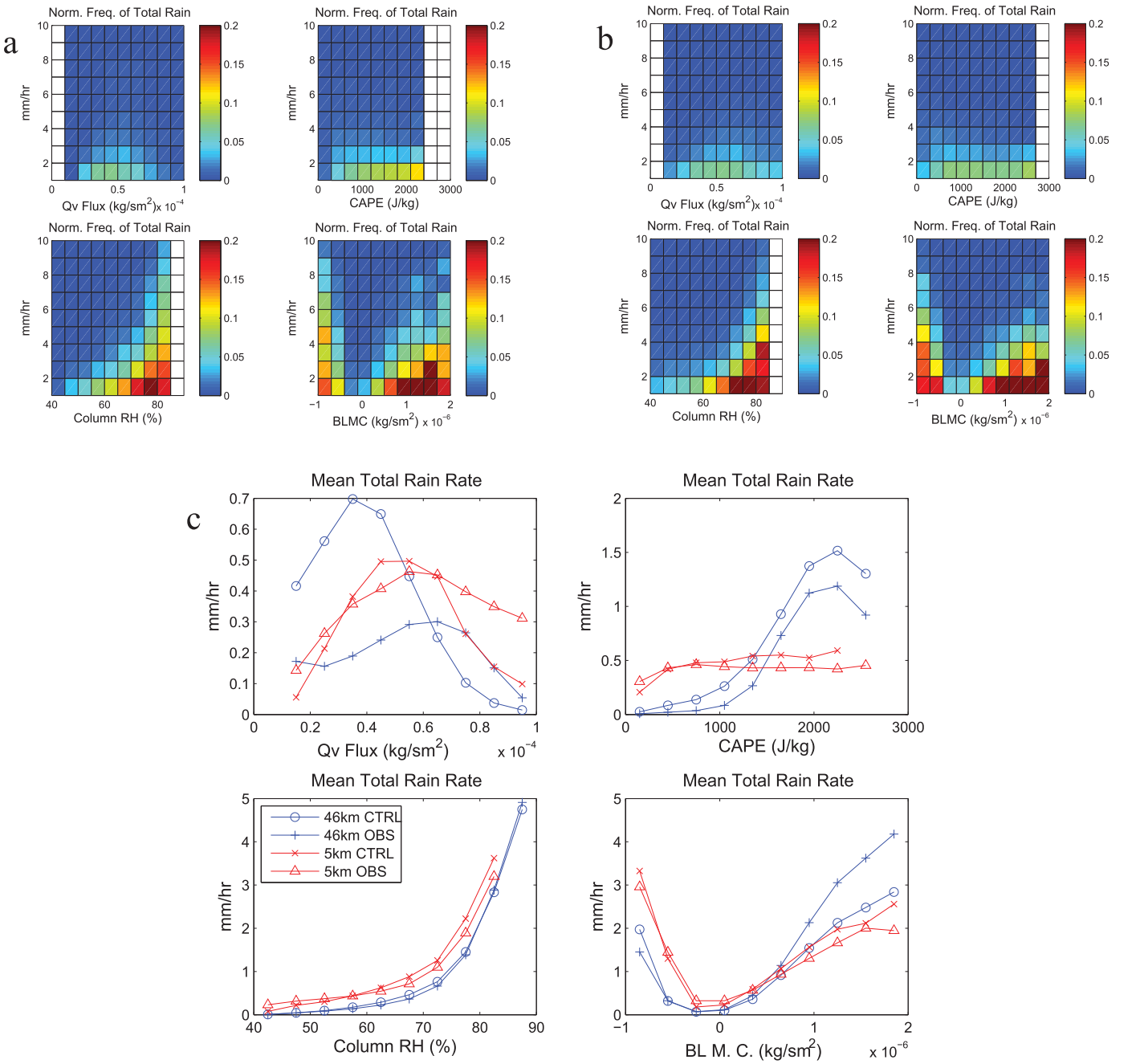

Figure 17. Normalized frequencies of total rain rate in the tropics for (a) the 5 km nested aquapatch with control SST profile; (b) 5 km nested aquapatch with observed SST profile; (c) results summarized in terms of mean rain rates for four different cases: 46 km control SST (blue o's); 46 km observed SST (blue +'s); 5 km control SST (red ×'s); 5 km observed SST (red triangles).

convective cells can be seen on the leading (north) edge of the band, while the lighter, stratiform rain areas are on the trailing (south) edge. Generally, the leading edges of the squall lines and their propagation are more easily seen in terms of the 2 m temperature (T_{2m}, a diagnostic output of the boundary layer scheme). The plots on the left side of Figure 18 show a sequence of images of T_{2m} from the 46 km grid (domain 1) for the 5 km nested aquapatch simulation with control SST. The plots are separated by 6 h, and the magenta arrows subjectively show the location and motion of squall lines propagating away from the equator. Such events occur repeatedly in this simulation. Vertical cross sections through these lines show cold pools that are typically about 500 m deep with temperature anomalies of −2 to −4 K, poleward boundary layer winds of 5–10 ms^{-1}, and precipitation falling on their leading edges (not shown).

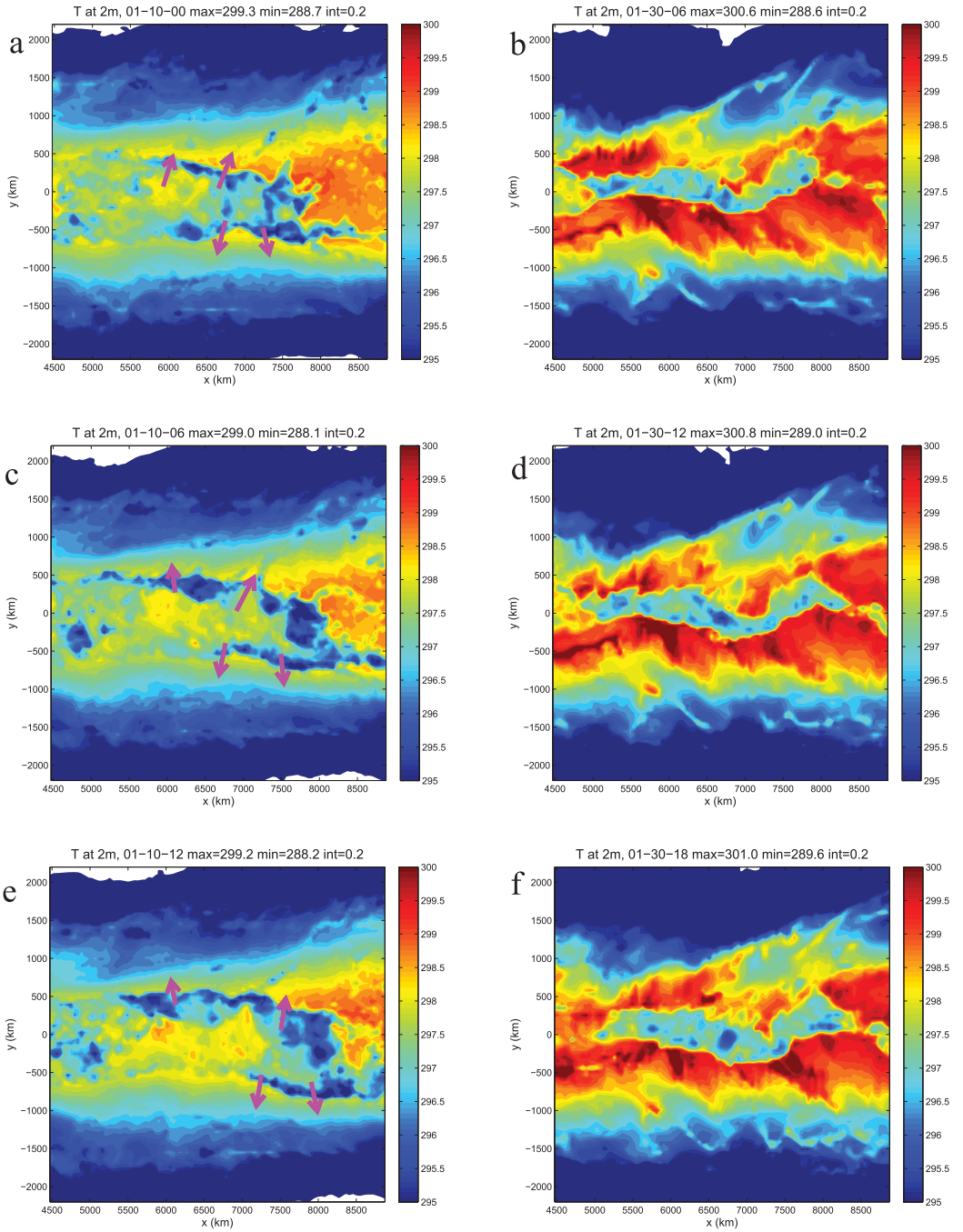

Figure 18. 2 m temperature over selected 12 h periods for (left) the 5 km nested control SST simulation and (right) the 46 km control SST simulation.

Meridionally propagating squall lines also occur for the 46 km simulation with CP, but they are generally weaker, shorter-lived, and do not travel as far. One of the more robust examples of cold pool/squall line propagation is shown in the plots on the right side of Figure 18. While the coldest T_{2m} values are as cold as the coldest values on the left, the areas of the coldest regions are much smaller. In the 12 h period, the edges of the larger cold pool region do not propagate as far to the north and south as for the example from the 5 km simulation.

To more objectively differentiate between precipitation that is or is not associated with meridional propagation, we compute space-time lag correlations. Specifically, using rain rate data saved every 3 h on the 46 km

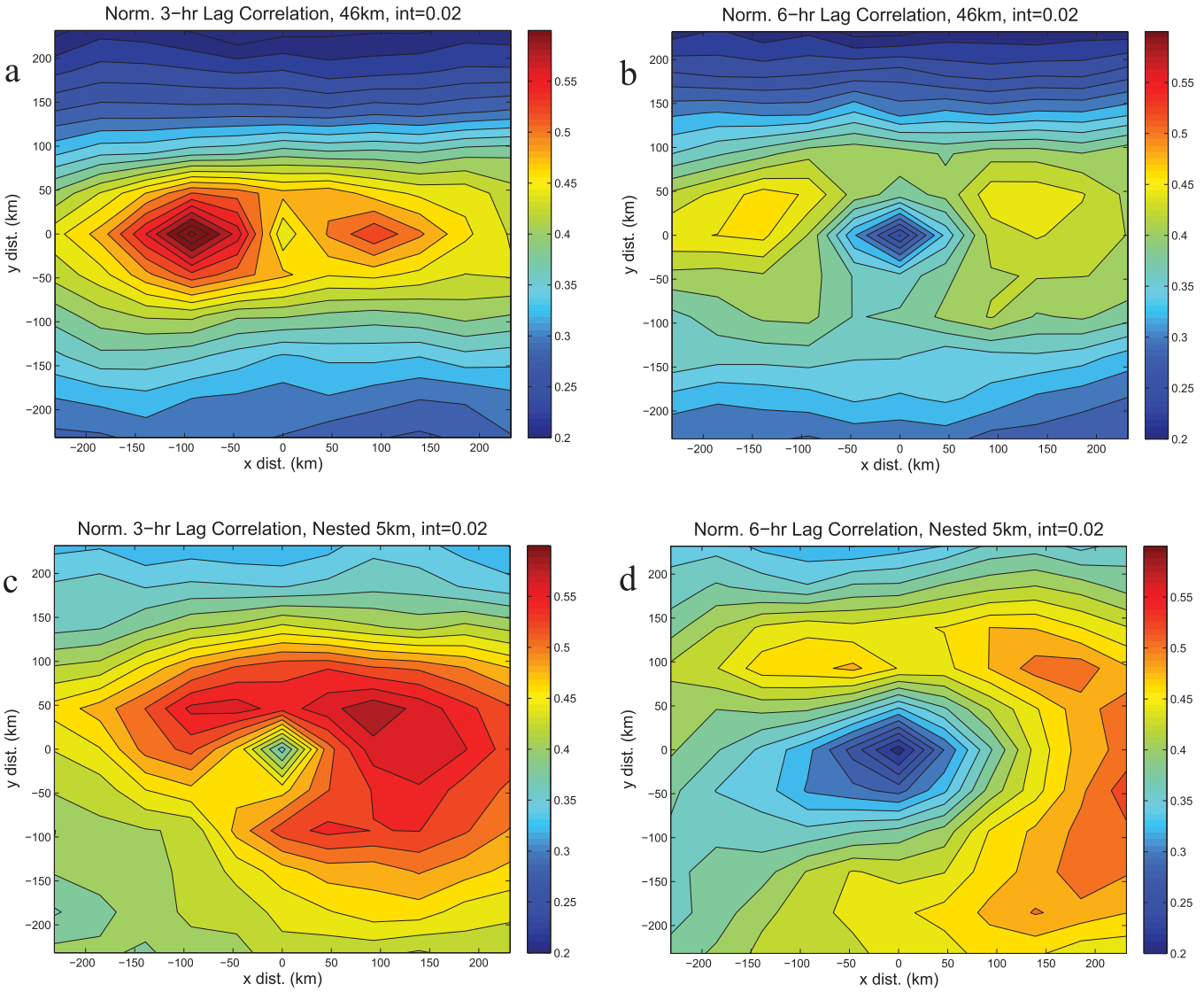

Figure 19. Normalized lag-correlations of rain rate between locations with rainfall rates greater than 1.0 mm h^{-1} and adjacent locations at subsequent times: (a) 46 km aquapatch, 3 h lag; (b) 46 km aquapatch, 6 h lag; (c) 5 km nested, 3 h lag; (d) 5 km nested, 6 h lag.

grid for both the 46 km aquapatch and nested 5 km with control SST, we identify every grid point between the equator and 10° north with rain rates greater than 1.0 mm h^{-1}. Using these as reference points, we compute the normalized correlation between their rain rates and the rain rates at nearby points, but at lags of 3 or 6 h. The normalization uses the combined variances at both the reference point and its neighbors, i.e.,

$$c_{i,j}(\tau)=\left\{\frac{1}{N}\sum r_{0,0}\times r_{i,j}(\tau)\right\}/\left\{\sigma_{0,0}\times\sigma_{i,j}\right\}^{1/2} \tag{4.1}$$

where the *r*s are rain rates, 0,0 refers to the reference point, *i* and *j* range from −5 to +5, *N* is the number of samples (over 100,000 for each case), τ is the lag, and σ is the variance of each location relative to reference points. For $\tau = 0$, $c_{0,0}$ converges to 1.0.

Figure 19 shows the results. For the 46 km aquapatch, the 3 h lag correlations show that significant rain rates are most often followed by rainfall directly to the west, and also to the east (though not as frequently). At 6 h, there is a hint of some propagation northward with time. For the nested 5 km simulation, at $\tau = 3$ h there are clear signals of propagation to the northwest, northeast, and also to the

southeast, with largest correlations at 46 km (one grid point) to the north. At $\tau = 6$ h, the propagation continues in all three directions. Further inspection of the rain rate and T_{2m} fields (not shown) finds that some squall lines actually propagate back across the equator, which explains the signals indicating southeastward propagation. It is evident that, in contrast to the 46 km simulation with CP, heavy rainfall in the ITCZ region of the 5 km simulation tends to propagate meridionally.

These findings of more pronounced squall line propagation are consistent with the earlier work of *Weisman et al*. [1997], who studied the simulated evolution of three-dimensional, quasi-linear squall lines in shear as a function of horizontal resolution. As the grid spacing was changed from 12 to 8 to 4 km the overall evolution became quite similar to their "ideal" case that used 1 km grid spacing. More importantly, *Weisman et al*. noted that the strengths of the surface cold pools and the resulting propagation of the squall lines increased considerably as the resolution was changed from 12 to 4 km, but did not increase much more for smaller grid spacings. Those simulations were performed without CP. However, as suggested by the results shown earlier using 15 km grid spacing both with and without CP (Figures 12 and 14), it is the decrease of grid spacing to 5 km leads to the most qualitatively different results.

4.3. Can the Tiedtke Scheme be Modified to Produce Similar Results?

One of the most important empirical parameters in many cumulus schemes is the entrainment parameter E which determines the rate at which rising or sinking columns of air mix with their surrounding environment. Large values of E tend to suppress convection in less favorable environments (e.g., less CAPE or lower CRH) because rising plumes become diluted by mixing with their environment as they rise. In the WRF 3.4.1 formulation of the Tietdke CP there are several entrainment parameters with the following default values: for penetrative (deep) convection, $E_{pen} = 1.0\text{x}10^{-4}$ m^{-1}; for midlevel (synoptically forced) convection, $E_{mid} = 1.0 \times 10^{-4}$ m^{-1}; for shallow convection, $E_{scv} = 1.2 \times 10^{-3}$ m^{-1}; and for downdrafts, $E_{dd} = 2.0 \times 10^{-4}$ m^{-1}. Another relevant parameter is the downdraft mass flux, which is the fraction of the detrained updraft mass flux that can be potentially converted into downdraft mass flux. Its default value is $C_{DMF} = 0.3$.

Using the 46 km aquapatch and the observed SST profile, we attempted to find modifications to these parameters that changed the pronounced double ITCZ configuration shown by the blue curve in Figure 14 to something more like the broader rainfall distribution of the 5 km nested simulation shown by the red curve. Since the normalized rainfall diagrams shown above indicate that the explicit convection is actually less sensitive to CAPE and CRH, lower values for E_{pen} seem like a logical starting point. However, as shown in Figure 20a, none of the results for values of $E_{pen} = 0.5$, 0.75, 1.5, or 1.75×10^{-4} m^{-1} produced rainfall distributions more similar to the 5 km results. Most of these rain-rate profiles are noisier than what has been shown above, in part because these results were computed from only the last 6 months of 18 month simulations. For $E_{pen} \leq 1.5 \times 10^{-4}$ m^{-1} there is a clear double ITCZ, but there is a single ITCZ for $E_{pen} = 1.75\text{x}10^{-4}$ m^{-1}. In fact, the change occurs across an even smaller range of E_{pen}, with double ITCZ for $E_{pen} = 1.5625 \times 10^{-4}$ m^{-1} and single ITCZ for $E_{pen} = 1.625 \times 10^{-4}$ m^{-1} (not shown). This outcome is consistent with the results of *Möbis and Stevens* [2012], who found that increasing the entrainment parameter made the convection away from the equator more susceptible to mixing with dry air from the subtropics, thus pushing the preferred precipitation region back toward the equator.

However, as E_{pen} is decreased to 0.75 and 0.5×10^{-4} m^{-1}, the simulated ITCZ does not broaden nor become more like the results of the nested 5km case in any way. It is evident that changing E_{pen} in either direction does not make the 46 km simulations with CP more like the 5 km results.

Since stronger cold pools seem to be evident in the 5 km simulations, we also considered whether increasing downdraft strengths would have a positive effect. In theory, downdrafts and their associated cold pools could be strengthened either by increasing the downdraft mass flux to C_{DMF} to 0.45, or by decreasing downdraft entrainment E_{dd} to 1.0×10^{-4} m^{-1}. However, as shown in Figure 20b, neither of these changes made the ITCZ more like the 5 km results, nor did applying them both at the same time (nor did changing either of those parameters in the other direction, not shown).

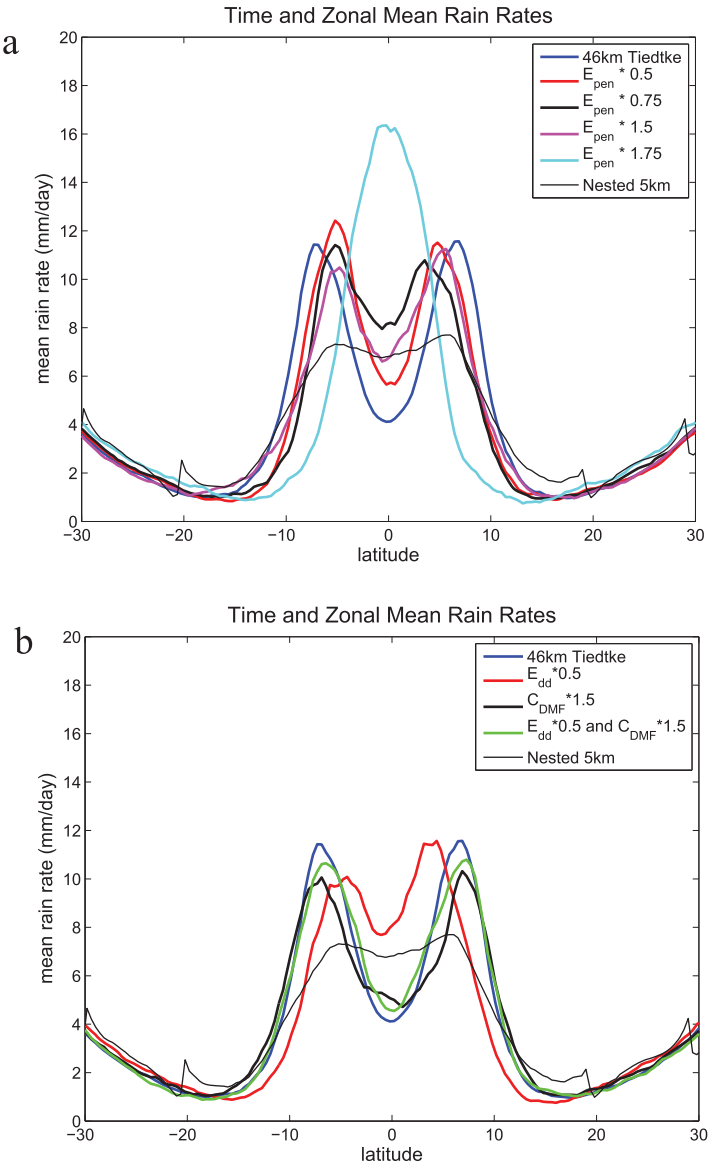

Figure 20. Rain rate profiles for simulations with modified entrainment parameters in the Tiedtke CP scheme: (a) results for changes in entrainment for penetrative (deep) convection; (b) results for changes to initial downdraft mass flux and entrainment for downdrafts. The new rain-rate profiles are somewhat noisier than what appears in previous figures because they were computed from only 6 months of model output.

5. Summary and Conclusions

The primary goal of this study was to develop a modeling framework in which simulated atmospheres using low to moderate resolution and CP, with realistic tropical and midlatitude dynamics, can be directly compared to the output of high-resolution simulations that do not use CP. In this case "high resolution" refers to 5 km grid spacing, which is by no means ideal and is not typically considered "cloud resolving." However, the simulations show significant changes in the precipitation distribution when the resolution is changed from 15 to 5 km, indicating that 5 km resolution leads to important changes in the dynamics of organized convection.

The framework proposed here uses the grid-nesting capabilities of an established community model (WRF) modified so that the nested grid boundaries can extend across the zonally periodic boundaries. Preliminary simulations without grid nesting were performed using the "aquachannel" configuration which is an equatorial beta-plane approximately equal in length to the entire Earth. "Aquapatch" simulations were similar but with a domain length equal to 1/3 the length of the equator. The tropical and midlatitude circulations and eddy statistics of these simulations were shown to compare satisfactorily with those of equivalent aquaplanet models. Another useful finding is that the majority of the rainfall in the midlatitudes was produced by explicit processes (see Figures 2 and 8), reducing the effects (or biases) of the choice of CP in those regions. This suggests that cloud-resolving grid spacings are most beneficial in the tropics and are not as critical in the midlatitudes.

Applying 5 km grid spacing without CP to the tropics significantly changed the distributions of precipitation. For the control SST profile of *Neale and Hoskins* [2001], a fairly narrow and intense ITCZ was changed to a weaker ITCZ and a broader distribution of rain. For the observed SST profile, a pronounced double ITCZ was changed to a marginal double ITCZ, again with a much broader distribution of light rain into the fringes of the tropics. Neither changes to the entrainment parameters in the

Tiedtke CP scheme nor using other CP schemes produced rainfall distributions that were similar to the 5 km results.

To understand these differences, normalized frequency distributions were computed for rain rates as a function of various environmental parameters such as CAPE, column relative humidity (CRH), and boundary layer moisture convergence (BLMC). Rainfall production in the 46 km simulations with CP were found to be fairly sensitive to CAPE and very sensitive to CRH, the latter being in good agreement with other modeling studies and observations. Significant rainfall was found to occur for both positive and negative BLMC. Examination of this result and separation into convective rain (CR) and explicit rain (ER) showed that these two signals indicate the occurrence of deep and stratiform convection, respectively.

In the cloud-resolving simulations, rainfall production was found to be different in two ways: first, there was much less sensitivity to CAPE, with average rain rates becoming roughly constant for CAPE values ranging from 500 to 2000 Jkg^{-1}. Second, there was less sensitivity to dryness of the midlevel atmosphere (as measured by CRH; results for 700–500 hPa relative humidity were similar). The first result indicates that precipitation will be less tightly focused where the CAPE is highest, in contrast with the CP results. The second result is consistent with how precipitation is spread more broadly away from the ITCZ in the 5 km simulations.

Further examination of the model output offered a phenomenological explanation for both of these differences. The 5 km simulations produce stronger cold pools and associated squall lines that frequently propagate away from the ITCZ. Occasionally, they propagate back across the equator. As the squall lines propagate away from the initial convective event, they both reduce the rain rate in the initiation region and increase rain rates away from the ITCZ. While modifications to the entrainment parameters of the Tiedtke CP scheme can lead to changes such as single versus double ITCZs, they could not reproduce the more robust squall lines and broader rainfall profiles of the 5 km simulations.

Given the large sensitivities of tropical rainfall to CP (see also the Appendix A), it seems likely that 5 km grid spacing produces much more accurate results, either for the hypothetical aquaplanet or for the real Earth. Nonetheless we must consider the possibility that 5 km grid spacing is too close to the "gray zone" between resolutions that are appropriate for CP and resolutions that do not need it, and that the 5 km results are biased in the opposite sense as the CP results. We can take encouragement from some studies that have found satisfactory behavior for resolutions around 4 km, such as for squall lines [*Weisman et al*., 1997] or radiative-convective equilibrium [*Pauluis and Garner*, 2006]. *Bryan and Morrison* [2012] also found that strengths of precipitation-driven cold pools are sensitive to grid spacing, with the cold pools becoming stronger when grid spacing was decreased from 4 km to 1 km, but then moderating again as spacing was decreased to 0.25 km. Although their idealized simulations were over land, their results suggest that further decrease in grid spacing would not diminish the stronger cold pools and the more robust propagation of squall lines in the nested simulations.

Further work is required to fully understand, and hopefully address, biases in tropical precipitation found with CP schemes when compared to cloud-resolving simulations. The modeling strategies presented here - the aquachannel, aquapatch, and the nested aquapatch - have been shown to be useful for this purpose. The simulations also produce convectively coupled equatorial waves, which will be the topic of a forthcoming paper.

Appendix

In this brief Appendix A we show the results of some aquapatch simulations with different CP schemes. Our purposes are to (1) illustrate the large sensitivity of ITCZ structure to CP, (2) show that none of the other CP schemes produce rainfall distributions similar to the 5 km nested results, and (3) show that the normalized frequency diagrams and average rainfall rates explain some differences among schemes.

Results are shown for the 46 km aquapatch with the observed SST profile, since in this configuration the large majority of the rain comes from CP, and a diversity of ITCZ structures are produced.

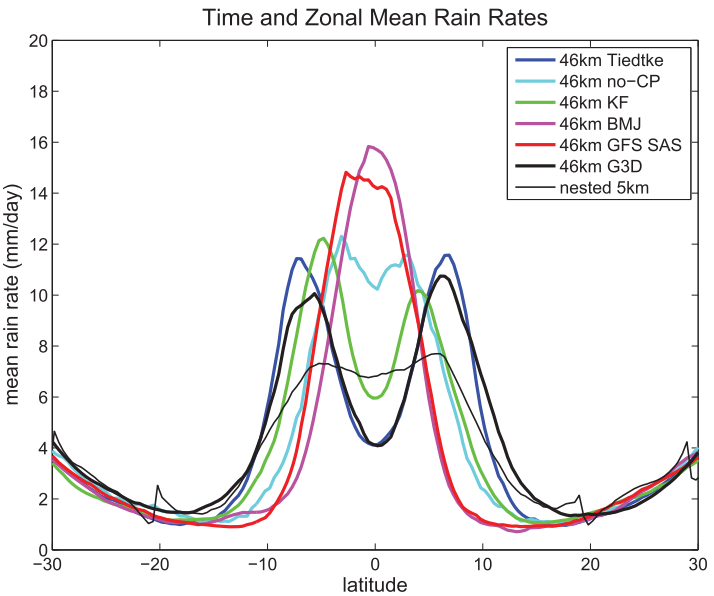

Figure A1. Time and zonal mean rain rate profiles for additional simulations using alternative cumulus parameterizations; see text for details.

Figure A1 shows rain rates in the tropics using the Kain-Fritsch (KF) [*Kain and Fritsch*, 1990; *Kain*, 2003], Betts-Miller-*Janjic* (BMJ) [*Betts and Miller*, 1986; *Janjic*, 1994], simplified Arakawa Schubert (SAS) [*Han and Pan*, 2011], and Grell 3D ensemble (G3D) [*Grell and Devenyi*, 2002] schemes, along with the original Tiedtke result, 46 km with no cumulus scheme (noCP), and the 5 km nested result. Most of these simulations were integrated for only 18 months and the averages were computed with only the last 6 months of data. This partially explains why some of the rainfall distributions are more asymmetrical and noisier than others; but only partly, because some of the simulations simply have more extreme rainfall events that lead to rougher mean profiles. This is particularly true for noCP, which by necessity generates many "gridpoint storms."

From the mean rain profiles we see that the KF and G3D schemes also produce robust double ITCZs. The KF and G3D schemes also generate numerous tropical-cyclone-like storms that emerge from either ITCZ and move into the midlatitudes (not shown); this did not occur in the simulations with Tiedtke CP. The no-CP simulation produces a marginal double ITCZ, somewhat like the nested 5 km result, except that the rain rates are greater and more narrowly focused on the equator, similar to the other 46 km results. SAS and BMJ produce single ITCZs, with rain rate profiles that are rougher and smoother, respectively.

Figure A2 shows normalized frequency diagrams for two of the schemes: KF and SAS. These two are shown because they illustrate some of the differences between the schemes that produce a double ITCZ (KF and G3D) and those that do not (BMJ and SAS). The most striking difference is in the lack of preference for high CAPE values for production of TR in the SAS scheme. The plot for BMJ was similar. Although less obvious, another difference is that for the SAS scheme, there is less rainfall for low values of CRH. BMJ was also similar in this regard (in comparison to KF and G3D).

Among the schemes, those that produce double ITCZs (including noCP) show a clear preference for producing more rain where CAPE is larger, while the two CP schemes that make single ITCZs generate the most of their rain with lower CAPE values. Reduced but still fairly high CAPE values often exist on both the poleward and equatorward sides of double ITCZs (not shown), but schemes that prefer higher CAPE and also have some sensitivity to midlevel dryness (in comparison to the nested 5 km results) will not produce significant rainfall in those regions. These differences can be seen more clearly from a plot with average total rain rates from each scheme (Figure A2c). The BMJ and SAS schemes produce less rain for low to moderate CRH but do not respond strongly to high CAPE values, while the KF and

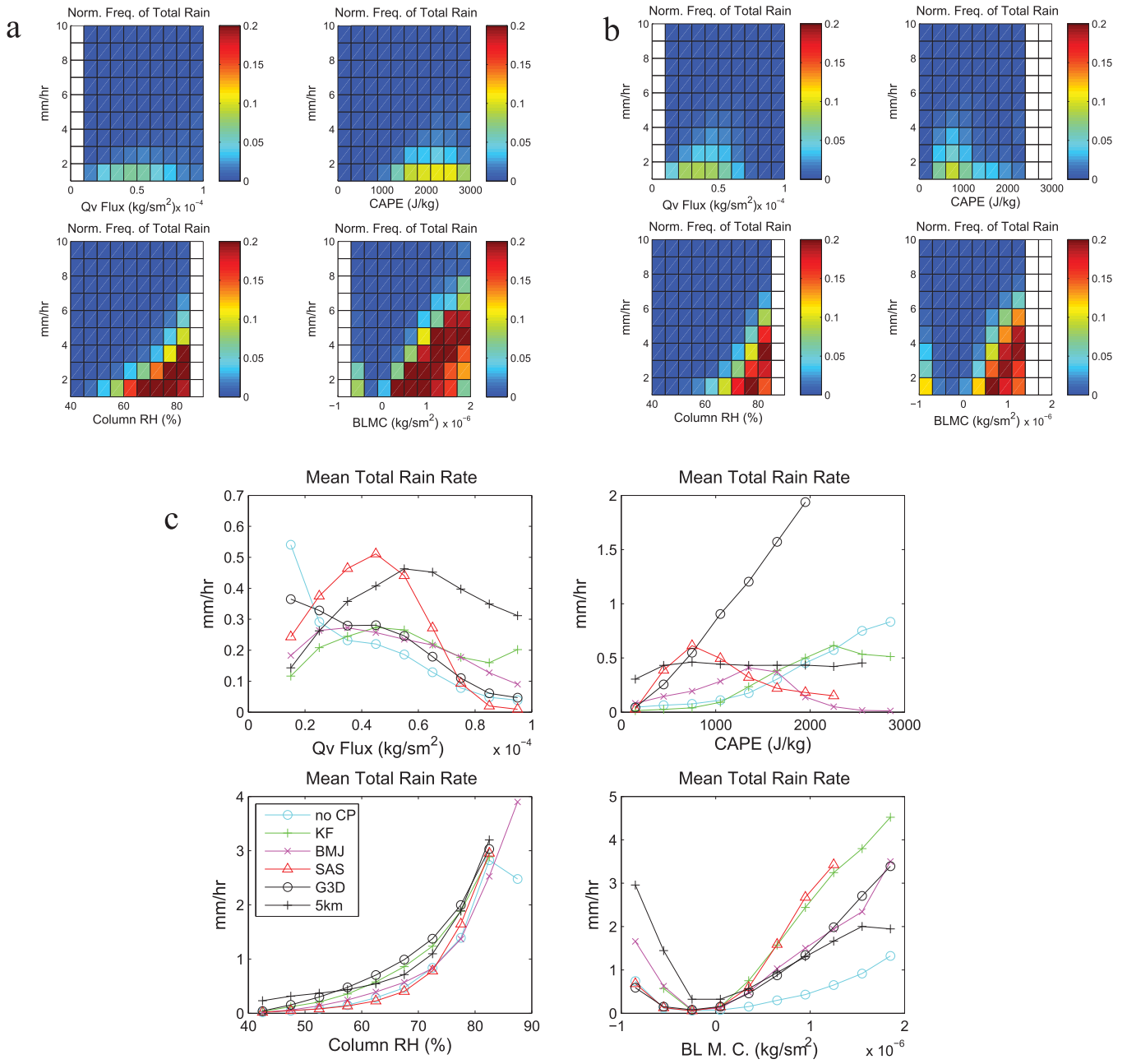

Figure A2. Normalized total rain rates as a function of environmental fields, for 46 km aquapatch simulations with the observed SST profile: (a) Kain-Fritsch; (b) simplified Arakawa-Schubert; (c) average total rain rates for each of the simulations with alternate CP schemes and the nested 5 km result.

G3D schemes are slightly less sensitive to dryness but are very productive in high CAPE. The nested 5 km simulations produce rainfall quite differently than all the CP schemes, being less sensitive to dryness and much less responsive to CAPE.

Acknowledgements
This work was supported by the National Science Foundation through grant AGS-1146701 and by the University of Miami. All resources for computations and data storage were provided by the UM Center for Computational Sciences. The authors would like to thank Michael Blackburn and David Williamson for assistance in obtaining and analyzing the Aqua-Planet Experiment data.

References

Betts, A. K., and M. J. Miller (1986), A new convective adjustment scheme. Part II: Single column tests using GATE wave, BOMEX, ATEX, and arctic air-mass data sets, *Q. J. R. Meteorol. Soc.*, *112*, 693–709.

Blackburn, M., and B. J. Hoskins (2013), Context and aims of the Aqua-Planet Experiment, *J. Meteorol. Soc. Jpn.*, *91A*, 1–15.

Blackburn, M., et al. (2013), The Aqua-Planet Experiment (APE): Control SST simulation, *J. Meteorol. Soc. Jpn.*, *91A*, 17–56.

Bretherton, C. S., and M. Khairoutdinov (2015), Convective self-aggregation feedbacks in near-global cloud-resolving simulations of an aquaplanet, *J. Adv. Model. Earth Syst.*, *7*, 1765–1787, doi:10.1002/2015MS000499.

Bretherton, C. S., M. E. Peters, and L. E. Back (2004), Relationships between water vapor path and precipitation over the tropical oceans, *J. Clim.*, *17*, 1517–1528.
Bryan, G. H., J. C. Wyngaard, and J. M. Fritsch (2003), Resolution requirements for the simulation of deep moist convection, *Mon. Wea. Rev.*, *131*, 2394–2416.
Bryan, G. B., and H. Morrison (2012), Sensitivity of a simulated squall line to horizontal resolution and parameterization of microphysics, *Mon. Weather Rev.*, *140*, 202–225.
Chou, M.-D., and M. J. Suarez (1999), A solar radiation parameterization for atmospheric studies, *NASA Tech. Rep. NASA/TM-1999-10460*, vol. 15, 38 pp.
Chou, M.-D., M. J. Suarez, C.-H. Ho, M. M.-H. Yan, and K-T. Lee (1998), Parameterizations for cloud overlapping and shortwave single-scattering properties for use in general circulation and cloud ensemble models, *J. Clim.*, *2*, 202–214.
Collins, M., et al. (2013) Long-term climate change: Projections, commitments, and irreversibility, *Climate Change 2013: The Physical Science Basis*, Contribution of Working Group I to the Fifth Assessment Report of the Intergovernmental Panel on Climate Change, edited by T. F. Stocker et al., chap. 12, 1535 pp., Cambridge Univ. Press, Cambridge, U. K.
Derbyshire, S. H., I. Beau, P. Bechtold, J.-Y. Grandpeix, J.-M. Piriou, J.-L. Redelsperger, and P. M. M. Soares (2004), Sensitivity of moist convection to environmental humidity, *Q. J. R. Meteorol. Soc.*, *130*, 3055–3079.
Fairall, C. W., E. F. Bradley, J. E. Hare, A. A. Grachev, and J. B. Edson (2003), Bulk parameterization of air–sea fluxes: Updates and verification for the COARE algorithm, *J. Clim.*, *16*, 571–591.
Grabowski, W. W. (2003), MJO-like coherent structures: Sensitivity simulations using the cloud-resolving convection parameterization (CRCP), *J. Atmos. Sci.*, *60*, 847–864.
Gregory, D., J.-J. Moncrette, C. Jakob, A. C. M. Beljaars, and T. Stockdale (2000), Revision of the convection, radiation, and cloud schemes in the ECMWF model, *Q. J. R. Meteorol. Soc.*, *126*, 2685–2710.
Grell, G. A., and D. Devenyi (2002), A generalized approach to parameterizing convection combining ensemble and data assimilation techniques, *Geophys. Res. Lett.*, *29*(14), 1693, doi:10.1029/2002GL015311.
Han, J., and H.-L. Pan (2011) Revision of convection and vertical diffusion schemes in the NCEP Global Forecast System, *Weather Forecasting*, *26*, 520–533.
Hayashi, Y.-Y., and A. Sumi (1986), The 30-40 day oscillation simulated in an "Aqua Planet" model, *J. Meteorol. Soc. Jpn.*, *64*, 451–465.
Held, I. M., and A. Y. Hou (1980), Nonlinear axially symmetric circulations in a nearly inviscid atmosphere, *J. Atmos. Sci.*, *37*, 515–533.
Held, I. M., and M. J. Suarez (1994), A proposal for the intercomparison of dynamical cores of atmospheric general circulation models, *Bull. Am. Meteorol. Soc.*, *75*, 1825–1830.
Hess, P. G., D. S. Battisti, and P. J. Rasch (1993), Maintenance of the intertropical convergence zones and the large-scale circulation on a water-covered Earth, *J. Atmos. Sci.*, *50*, 691–713.
Holloway, C. E., and J. D. Neelin (2009), Moisture vertical structure, column water vapor, and tropical deep convection, *J. Atmos. Sci.*, *66*, 1665–1683.
Hong, S.-Y., Y. Noh, and J. Dudhia (2006), A new vertical diffusion package with an explicit treatment of entrainment processes, *Mon. Weather Rev.*, *134*, 2318–2341.
Houghton, J. T., and G. J. Jenkins, and J. J. Ephraums (Eds.) (1990), *Climate Change: The IPCC Scientific Assessment*, 410 pp., Cambridge Univ. Press, Cambridge, U. K.
Janjic, Z. I. (1994), The step-mountain eta coordinate model: Further developments of the convection, viscous sublayer, and turbulence closure schemes, *Mon. Weather Rev.*, *122*, 927–945.
Kain, J. S. (2003), The Kain-Fritsch convective parameterization: An update, *J. Appl. Meteorol.*, *43*, 170–181.
Kain, J. S., and J. M. Fritsch (1990), A one-dimensional entraining/detraining plume model and its application in convective parameterization, *J. Atmos. Sci.*, *47*, 2784–2802.
Khoudier, B., and Y. Han (2013), Simulation of convectively coupled waves using WRF: A framework for assessing the effects of mesoscales on synoptic scales, *Theor. Comput. Fluid Dyn.*, *27*, 473–489.
Kiladis, G. N., M. C. Wheeler, P. T. Haertel, K. H. Straub, and P. E. Roundy (2009), Convectively coupled equatorial waves, *Rev. Geophys.*, *47*, RG2003, doi:10.1029/2008RG000266.
Kirtman, B., et al. (2013), Near-term climate change: Projections and predictability, *Climate Change 2013: The Physical Science Basis, Contribution of Working Group I to the Fifth Assessment Report of the Intergovernmental Panel on Climate Change*, edited by T. F. Stocker et al., chap. 11, 1535 pp., Cambridge Univ. Press, Cambridge, U. K.
Kirtman, B. P., and E. K. Schneider (2000), A spontaneously generated tropical atmospheric circulation, *J. Atmos. Sci.*, *57*, 2080–2093.
Liu, Y., L. Guo, W. Guoxiong, and Z. Wang (2010), Sensitivity of ITCZ configuration to cumulus convective parameterizations on an aquaplanet, *Clim. Dyn.*, *34*, 223–240.
Manabe, S., and R. T. Wetherald (1975), The effects of doubling the CO2 concentration on the climate of a General Circulation Model, *J. Atmos. Sci.*, *32*, 3–15.
Medeiros, B., B. Stevens, I. M. Held, M. Zhao, D. L. Williamson, J. G. Olson, and C. S. Bretherton (2008), Aquaplanets, climate sensitivity, and low clouds, *J. Clim.*, *21*, 4974–4991.
Medeiros, B., B. Stevens, and S. Bony (2014), Using aquaplanets to understand the robust responses of comprehensive climate models to forcing, *Clim. Dyn.*, *39*, 1–20.
Miyamoto Y, Y. Kakijawa, R. Yoshida, T. Yamamura, H. Yashiro, and H. Tomito (2013), Deep moist atmospheric convection in a subkilometer global simulation, *Geophys Res. Lett.*, *40*, 4922–4926, doi:10.1002/grl.50944.
Möbis, B., and B. Stevens (2012), Factors controlling the position of the Intertropical Convergence Zone on an aquaplanet, *J. Adv. Model. Earth Syst.*, *4*, M00A04, doi:10.1029/2012MS000199.
Morrison, H. (2016), Impacts of updraft size and dimensionality on the perturbation pressure and vertical velocity in cumulus convection, Part 1: Simple, generalized analytic solutions, *J. Atmos. Sci.*, doi:10.1175/JAS-D-14-0066.1, in press.
Nasuno, T. (2008), Equatorial mean zonal wind in a global nonhydrostatic aquaplanet experiment, *J. Meteorol. Soc. Jpn.*, *86A*, 219–236.
Nasuno, T., H. Tomita, S. Iga, H. Miura, M. Satoh (2007), Multi-scale organization of convection simulated with explicit cloud processes on an aquaplanet, *J. Atmos. Sci.*, *64*, 1902–1921.
Neale, R. B., and B. J. Hoskins (2001), A standard test for AGCMs including their physical parameterizations. I: The proposal, *Atmos. Sci. Lett.*, *1*, doi:10.1006/asle.2000.0019.
Nolan, D. S., C. Zhang, and S.-H. Chen (2007), Dynamics of the shallow meridional circulation around intertropical convergence zones, *J. Atmos. Sci.*, *64*, 2262–2285.

Nolan, D. S., S. W. Powell, C. Zhang, and B. E. Mapes (2010), Idealized simulations of the Intertropical Convergence Zone and its multi-level circulations, *J. Atmos. Sci.*, *67*, 4028–4053.
Numaguti, A. (1995), Dynamics and energy balance of the Hadley circulation and the tropical precipitation zones. Part II: Sensitivity to meridional SST distribution, *J. Atmos. Sci.*, *52*, 1128–1141.
Pauluis, O., and S. Garner (2006), Sensitivity of radiative–convective equilibrium simulations to horizontal resolution, *J. Atmos. Sci.*, *63*, 1910–1923.
Peters, O., and J. D. Neelin (2006), Critical phenomena in atmospheric precipitation, *Nat. Phys.*, *2*, 393–396.
Pike, A. C. (1971), Intertropical convergence zone studied with an interacting atmosphere and ocean, *Mon. Weather Rev.*, *99*, 469–477.
Randall, D. A. (Ed.) (2000), *General Circulation Model Development. Past, Present, and Future*, 807 pp., Academic, Cambridge, Mass.
Satoh, M. (2014), *Atmospheric Circulation Dynamics and General Circulation Models*, 730 pp., Springer, Berlin.
Satoh, M., T. Matsuno, H. Tomita, H. Miura, T. Nasuno, S. Iga (2008), Nonhydrostatic Icosahedral Atmospheric Model (NICAM) for global cloud resolving simulations, *J. Comput. Phys.*, *227*, 3486–3514, doi:10.1016/j.jcp.2007.02.006.
Schneider, E. K. (1977), Axially symmetric steady-state models of the basic state for instability and climate studies. Part II: Nonlinear calculations, *J. Atmos. Sci.*, *34*, 280–297.
Skamarock, W. C., J. B. Klemp, J. Dudhia, D. O. Gill, D. M. Barker, M. G. Duda, X.-Y. Huang, W. Wang, and J. G. Powers (2008), A description of the advanced research WRF Version 3, *NCAR Tech. note 475+STR*, 113 pp.
Skamarock, W. C., S.-H. Park, J. B. Klemp, and C. Snyder (2014), Atmospheric kinetic energy spectra from global high-resolution nonhydrostatic simulations, *J. Atmos. Sci.*, *71*, 4369–4381.
Sumi, A. (1992), Pattern formation of convective activity over the aqua-planet with globally uniform sea surface temperature (SST), *J. Meteorol. Soc. Jpn.*, *70*, 855–875.
Tao, W.-K., et al. (2003), Microphysics, radiation and surface processes in the Goddard Cumulus Ensemble (GCE) model, *Meteorol. Atmos. Phys.*, *82*, 97–137.
Tiedtke, M. (1989), A comprehensive mass flux scheme for cumulus parameterization in large-scale models, *Mon. Weather Rev.*, *117*, 1779–1800.
Tompkins, A. M. (2001). Organization of tropical convection in low vertical wind shears: The role of water vapor, *J. Atmos. Sci.*, *58*, 529–545.
Tulich, S. N., and G. N. Kiladis (2012), Squall lines and convectively coupled gravity waves in the tropics: Why do most cloud systems propagate westward?, *J. Atmos. Sci.*, *69*, 2995–3012.
Wang, Y., L. Zhou, and K. Hamilton (2007), Effect of convective entrainment/detrainment on the simulation of the tropical precipitation diurnal cycle, *Mon. Weather Rev.*, *135*, 567–585.
Weisman, M. L., W. C. Skamarock, and J. B. Klemp (1997), The resolution dependence of explicitly modeled convective systems, *Mon. Weather Rev.*, *125*, 527–548.
Wheeler, M., and G. N. Kiladis (1999), Convectively coupled equatorial waves: Analysis of clouds and temperature in the wavenumber-frequency domain, *J. Atmos. Sci.*, *56*, 374–399.
Williamson, D. L., et al. (2012), The APE Atlas, *NCAR Tech. Note NCAR/TN-484+STR*, xxii+508 pp., Natl. Cent. for Atmos. Res., Boulder, Colo.
Williamson, D. L., et al. (2013), The Aqua-Planet Experiment (APE): Response to changed meridional SST profile, *J. Meteorol. Soc. Jpn.*, *81A*, 57–89.